Laser Ionization Mass Analysis

Edited by

AKOS VERTES

George Washington University
Washington, D.C.

RENAAT GIJBELS
FRED ADAMS

University of Antwerp (UIA)
Antwerp, Belgium

A WILEY-INTERSCIENCE PUBLICATION

JOHN WILEY & SONS, INC.

New York / Chichester / Brisbane / Toronto / Singapore

CHAPTER

4

THE HIGH LASER IRRADIANCE REGIME

*A. LASER ABLATION AND PLASMA FORMATION**

CLAUDE R. PHIPPS

Chemical and Laser Sciences Division
Los Alamos National Laboratory
Los Alamos, New Mexico

RUSSELL W. DREYFUS

IBM Research Division
T. J. Watson Research Center
Yorktown Heights, New York

4A.1. PLASMA-MEDIATED LASER–TARGET COUPLING AT IRRADIANCE GREATER THAN 1 GW/cm^2

4A.1.1. Introduction

The present section treats the specialized physics of high-irradiance vacuum target coupling. The reader is cautioned that this specialization restricts our attention to situations that meet our definition of "high irradiance" outlined in Section 4A.1.3, below. This restriction prevents us from reviewing experiments in air, in materials that absorb in depth rather than on the surface, and those that occur below the plasma threshold. Our focus on surface absorbers is consistent with the limitation to high irradiance, since it can be shown that *all* absorbers in vacuum coalesce to the behavior of surface absorbers at high irradiance. We also avoid discussing work with picosecond and shorter pulses, because the interaction physics is still poorly understood. Often, we have had to exclude data where the irradiance was not clearly specified. In return for these restrictions, our specialized purview has the advantage that it permits

* Dedicated to Professor Heinrich Hora on his sixtieth birthday.

Laser Ionization Mass Analysis, Edited by Akos Vertes, Renaat Gijbels, and Fred Adams. Chemical Analysis Series, Vol. 124.
ISBN 0-471-53673-3

us to theoretically predict all the main features of the majority of high-irradiance ablation data available at this time.

For consideration of the vast store of data taken in physical regimes outside the range we consider here, the reader is referred to other chapters in this volume. Discussion of RIMS elemental analysis appears in Dietze and Becker's contribution (Part C of this chapter, Section 4C.2.2).

By definition, the high-irradiance regime features a laser–surface interaction dominated by a plasma layer that forms just above the surface. For this reason, the observables of the interaction depend less on the chemical or molecular composition of the preirradiation solid material and more on the simple atomic abundances and ion charge states present in the ablation plume. The photoinitiated plasma layer near the target surface is mainly responsible for laser absorption and quickly redistributes the incident energy into thermal conduction and reradiation (with the radiation spectrum of the plasma, rather than of the laser), which actually communicate energy to the solid surface.

The present discussion aims at showing that most aspects of high-irradiance laser–surface interaction in vacuum—such as pressure, plasma density, and ion velocity—can be predicted quite well from plasma physics theory. The physical and chemical properties of the underlying solid material enter as average ionic mass number, A, and average ionic charge, Z, in the ablation plume, evaluated close to the region where laser absorption occurs. As an example, for KrF lasers with $\tau = 10$ ns and target irradiance $\approx 10\,\mathrm{GW/cm^2}$, vacuum ablation pressures can be tens of kilobars, and temperatures on the order of 50,000 K. It is obvious that molecular and even chemical structure in the ablated target material are destroyed early in such interactions.

Here, in Section 4A.1, we define the boundary to this case in terms of the range of laser irradiation parameters which occur in laser ionization mass analysis, and outline the theory for the limiting case of high irradiance. In Section 4A.2, we compare predictions to experimental results. Section 4A.3 treats ion acceleration, and Section 4A.4 considers measurement techniques. Section 4A.5 presents our conclusions.

Why Does High Irradiance in LIMA Work? Above $5\,\mathrm{GW/cm^2}$ irradiance, the ionization fraction approaches unity (e.g., Bingham and Salter, 1976a,b), whereas it can be 10^{-2}–10^{-3}, or even lower, with 1 decade less irradiance. A high source flux is a benefit for laser ionization mass analysis (LIMA) work. High irradiance around $1\,\mathrm{GW/cm^2}$ ($20\,\mathrm{TW/m^2}$) also makes for more uniform relative sensitivity coefficients (RSC) (Conzemius and Capellen, 1980; Ramendik et al., 1987). Mass resolution $\geqslant 300$ together with a 10^{-3} transmission coefficient are conditions commonly achieved at $10\,\mathrm{GW/cm^2}$ irradiance ($100\,\mathrm{TW/m^2}$) (Eloy, 1974), and values up to 1500 at this irradiance are indicated (Kovalev et al., 1978). For elemental analysis, higher resolution is not required.

Table 4A.1. Basic Constants and Units Used

Quantity	Symbol	cgs	SI
Absorption coefficient	α	$\mathrm{cm^{-1}}$, $\times 100 =$	$\mathrm{m^{-1}}$
Light speed	c	2.998×10^{10} cm/s	2.998×10^{8} m/s
Specific heat (practical)	C	$\mathrm{J \cdot g^{-1} \cdot K^{-1}}$, $\times 10^{3} =$	$\mathrm{J \cdot kg^{-1} \cdot K^{-1}}$
Electric field strength (physical)	E	esu/cm, $\times 29{,}979 =$	V/m
Electric field strength (practical)	E	V/cm, $\times 100 =$	V/m
Electron charge	e	4.803×10^{-10} esu	1.602×10^{-19} C
Free-space permittivity	ε_0	1 esu	8.854×10^{-12} F/m
Fluence (physical)	Φ	$\mathrm{erg/cm^2}$, $\times 10^{-13} =$	$\mathrm{J/m^2}$
Fluence (practical)	Φ	$\mathrm{J/cm^2}$, $\times 10^{4} =$	$\mathrm{J/m^2}$
Planck's constant	h	6.6256×10^{-27} erg·s	6.6256×10^{-34} J·s
Planck's constant	$\hbar$	$h/2\pi$	$h/2\pi$
Viscosity	η	$\mathrm{cm^2/s}$, $\times 10^{4} =$	$\mathrm{m^2/s}$
Volumetric irradiance (practical)	i	$\mathrm{W/cm^3}$, $\times 10^{6} =$	$\mathrm{W/m^3}$
Irradiance (physical)	I	erg $\mathrm{cm^{-2}s^{-1}}$, $\times 10^{-3} =$	$\mathrm{W/m^2}$
Irradiance (practical)	I	$\mathrm{W/cm^2}$, $\times 10^{4} =$	$\mathrm{W/m^2}$
Momentum	J	dyn·s, $\times 10^{-5} =$	n·s
Boltzmann's constant	k	1.3805×10^{-16} erg/K	1.3805×10^{-23} J/K
Thermal conductivity (practical)	K	W/cm, $\times 100 =$	W/m
Thermal diffusivity	κ	$\mathrm{cm^2/s}$, $\times 10^{-4} =$	$\mathrm{m^2/s}$
Wavelength	λ	cm, $\times 0.01 =$	m
Mach number	M	Dimensionless	Dimensionless
Electron mass	m_e	9.1091×10^{-28} g	9.1091×10^{-31} kg
Proton mass	m_p	1.673×10^{-24} g	1.673×10^{-27} kg
Particle density	n	$\mathrm{cm^{-3}}$, $\times 10^{6} =$	$\mathrm{m^{-3}}$
Potential	ϕ	esu, $\times 299.79 =$	V
Pressure (physical)	p	$\mathrm{dyn/cm^2}$, $\times 0.1 =$	Pa
Pressure (practical)	p	bar, $\times 10^{-5} =$	Pa
Mass density	ρ	$\mathrm{g/cm^3}$, $\times 10^{3} =$	$\mathrm{kg/m^3}$
Stefan–Boltzmann constant	σ	$5.67 \times 10^{-12}\,\mathrm{W \cdot cm^{-2} \cdot K^{-4}}$	$5.67 \times 10^{-8}\,\mathrm{W \cdot m^{-2} \cdot K^{-4}}$
Temperature (physical)	T	K	K
Temperature (practical)	T	eV, $\times 11{,}605 =$	K
Energy	W	erg, $\times 10^{-7} =$	J (joule)

Units. Equations are written alternately in practical cgs and SI units throughout this work, to conform to the broadly accepted SI convention while maintaining connection with the laser and plasma literature, which almost exclusively uses practical cgs. In the latter convention, physics is done in cgs but some common parameters are expressed in practical form. For example, temperature will be shown in kelvin units (K), and the electron charge will be in electostatic units (esu), but irradiance will be given in W/cm^2 rather than $erg \cdot cm^{-2} \cdot s^{-1}$ (see Table 4A.1). Occasional exceptions designed to make a specific point [e.g., electron volts (eV) in Eq. (18)] are clearly noted. Power-of-ten prefixes we use are f (10^{-15}), p (10^{-12}), n (10^{-9}), μ (10^{-6}), m (10^{-3}), k (10^{3}), M (10^{6}), G (10^{9}), T (10^{12}), and P (10^{15}).

4A.1.2. Basic Concepts: Survey of the Four Interaction Regions

Figure 4A.1 outlines the extremely wide range of plasma physics variables that are important in a pulsed laser–surface irradiation event in vacuum. The notation "not drawn to scale" cautions the reader that it is impossible to draw this illustration in a universally applicable way. The horizontal axis is approximately logarithmic. The distances and other parameters indicated across the top are dependent on scale lengths in a particular problem, and may vary by some orders of magnitude, depending on parameters such as laser pulse duration, τ, and irradiance. The specific numbers chosen for the illustration are typical of 100 μm diameter irradiation on aluminum, using 10–100 ns excimer laser pulses at 5–10 J/cm^2 (50–100 kJ/m^2).

Figure 4A.1 is meant to illustrate a sequence for plasma expansion into the vacuum and hence does not necessarily represent an achievable "snapshot" at any particular instant. Rather, it represents phenomena that are dominant near the plume density maximum, as the ablated material expands through many decades of decreasing density. For example, the laser may be "off" before the hot ion beam reaches Region IV, but such a situation does not refute any arguments we shall present.

Region I. Most of the laser absorption occurs in a thin plasma layer close to the target in Region I. Steady expansion away from the target in vacuum reduces the plasma density far below n_{ec} (see below) as distance from the target increases, leaving a narrow high-pressure zone close to the target where most absorption occurs. "Thin" in this context means a layer that is significantly smaller than the laser spot diameter [see Section 4A.1.5 (*Inverse Bremsstrahlung Absorption*...), below].

The absorption zone is close to the target because that is where the electron density first reaches the so-called critical density, n_{ec}. This density is called "critical" in plasma physics because, as it is approached, the complex magnitude

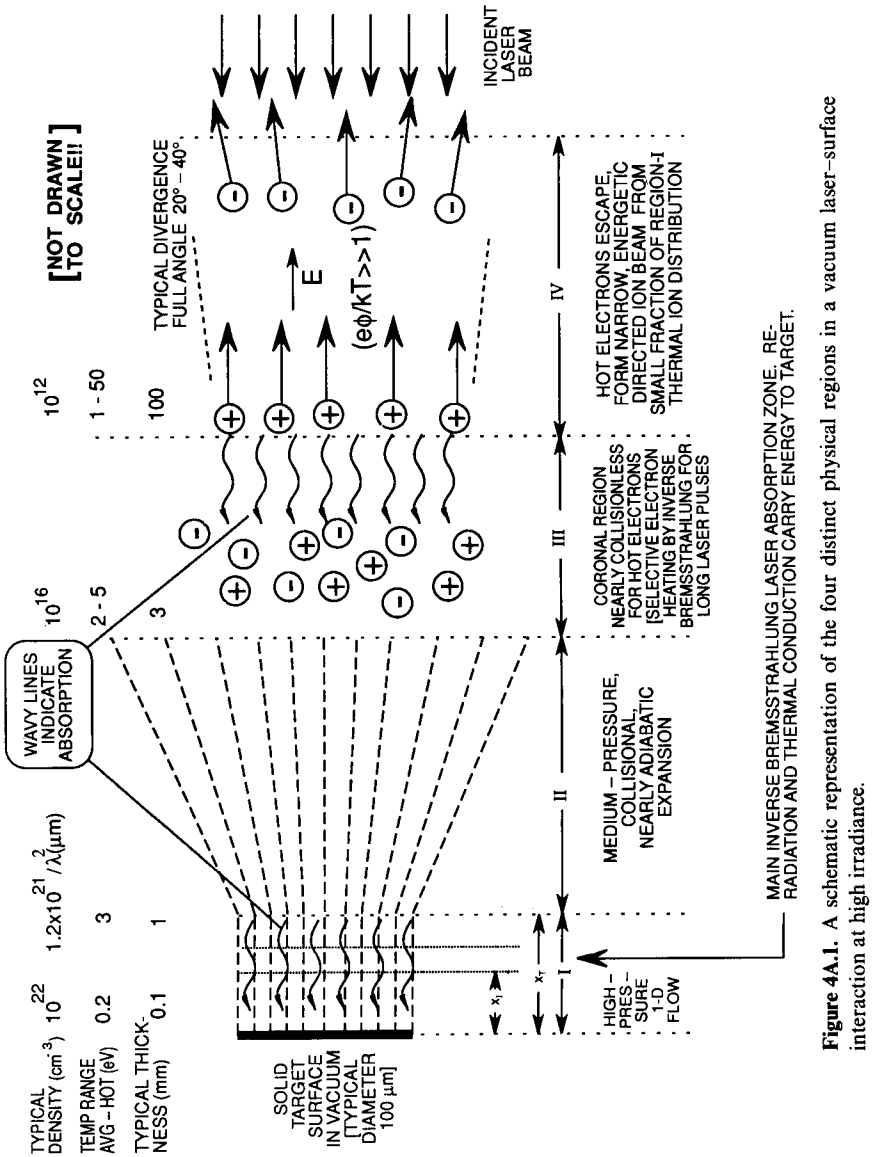

Figure 4A.1. A schematic representation of the four distinct physical regions in a vacuum laser–surface interaction at high irradiance.

of the plasma index of refraction decreases from near 1 to 0, first causing strong absorption, then total reflection of the incident light. The critical density has a very large, near-solid value (10^{21}–$10^{23}\,\mathrm{cm}^{-3}$ or 10^{27}–$10^{29}\,\mathrm{m}^{-3}$) for visible laser wavelengths and is high enough to create target surface pressures on the order of 100 kbar for KrF lasers (248 nm wavelength) and 2 eV temperature. It is related to other parameters by

$$n_{ec} = m_e \boldsymbol{n}^2 \omega^2 / 4\pi e^2 = 1.115 \times 10^{13}/\lambda^2 \quad \mathrm{cm}^{-3}$$

or (1)

$$n_{ec} = m_e \varepsilon_0 \boldsymbol{n}^2 \omega^2 / e^2 = 1.115 \times 10^{15}/\lambda^2 \quad \mathrm{m}^{-3}$$

In Eq. (1), $\boldsymbol{n}$ is the refractive index of the surrounding medium, which is taken as 1.0 on the right-hand side of Eq. (1) and throughout this work, and ω is the laser frequency (in radians).

It can be shown by integration from infinity [see Section 4A.1.5 (*Inverse Bremsstrahlung Absorption...*), below] and, with proper assumptions about the variation $n_e(x)$ with distance x, from the target surface that the effective thickness of the absorption zone is about $1/\alpha$, where α is the inverse bremsstrahlung absorption coefficient discussed in subsequent sections [i.e., absorption due to inelastic scattering of photons by free electrons (see Spitzer, 1967)]. The equivalent thickness of the absorption zone can be as small as a laser wavelength. For example, with a KrF laser, 2 eV plasma temperature, and $n_e = 0.2\, n_{ec} = 3.3 \times 10^{21}\,\mathrm{cm}^{-3}$ ($3.3 \times 10^{27}\,\mathrm{m}^{-3}$), $1/\alpha = \lambda = 248$ nm.

Even with very small laser spots, the physics governing *laser coupling* can be "one-dimensional" [see Section 4A.1.6 (*Heat Conduction and Reradiation*), below], despite the fact that, in free space, all expansions *eventually* become multidimensional. We call the distance at which the transition to multidimensional flow occurs x_T. It is the ratio of x_T to the irradiated diameter d_s that determines the "dimensionality" of the expansion after laser coupling has occurred.

Region II and the Knudsen Layer. In Region II, the expansion inevitably takes on a three-dimensional character. Naively, one might expect a hemispherical, bubble-like expansion into vacuum. However, even below the plasma threshold, the expansion of vapor from a half-plane has more of the character of a beam than a hemisphere, as was shown by Kelly and Dreyfus (1988a). This is because, in a highly collisional regime like Region I/II, a so-called *Knudsen layer* will form. In this layer, an explicit center-of-mass velocity develops, producing a beam-like expansion. It also produces a *reduced temperature* and *number density*, a consequence of collisional expansion of a Maxwellian velocity distribution of particles from an infinite half-plane (traveling with the center of mass).

The Kelly and Dreyfus derivation slightly underestimates the short-pulse collimation, as an additional cosine factor does not appear in such a steady-state derivation, i.e., a cosine term that resembles the case of collisionless vaporization into a vacuum or Knudsen nozzle expansion—the effective difference being, however, that the "vaporization" is from the dense medium in Region I.

The Knudsen layer will always be present in laser–target interactions that we consider, since sufficient (3–5) collisions to cause inverse bremsstrahlung absorption are also sufficient to form the Knudsen layer. The beam-like qualities of a Knudsen-layer expansion do not by themselves explain the features of *ion* beam formation in laser ablation, which we shall discuss in Section 4A.3.

Kelly and Dreyfus (1988a) show that the beamlike character of the expansion as it leaves the target in Region II is at least as sharply peaked in the forward direction as $\cos^4\theta$ and that an unsteady adiabatic expansion (such as in Region II) will produce a forward peaking more like $\cos^9\theta$. The latter distribution has $\theta_d = 44°$ full width at half-maximum (fwhm), and not $\theta_d = 90°$, as one finds for a "free" expansion.

Many examples of this forward peaking have been reported. Viswanathan and Hussla (1986) irradiated copper with a KrF laser in vacuum at 450 MW/cm^2, and saw forward peaking with an fwhm of about 45°, which was fit with a $\cos^8\theta$ distribution. At much higher laser fusion intensities, Mulser et al. (1973) irradiated a solid deuterium target with a Nd:glass laser at about 1 TW/cm^2 (10 PW/m^2) and obtained an angular flux dependence varying approximately as $\cos^5\theta$.

In any case, we take

$$(90/\theta_d) d_s = x_T \tag{2}$$

as the boundary beyond which the dimensionality of the free expansion is assumed to be >1. In Region II, an adiabatic expansion occurs, with a predicted variation

$$n(x)/n(x_T) = (x/x_T)^{-20/9} \tag{3}$$

for the ion or electron density with distance, x, from the target [see Puell, 1970; and Section 4A.1.6 (*Adiabatic Expansion Theory...*), below]. We note that von Gutfeld and Dreyfus (1989) observed an ion current variation

$$I_i(x) \propto (x/x_T)^{-2.5} \tag{4}$$

giving an experimentally determined exponent that agrees with the ion density profile predicted by adiabatic expansion theory to within 10%.

Three-body recombination (see Section 4A.1.5, below) is usually important in Regions I and II but ceases to be an important electron energy loss and atom-heating mechanism beyond the boundary between Regions II and III. Where ion densities n_i reach about $10^{18}\,\mathrm{cm}^{-3}$ ($10^{24}\,\mathrm{m}^{-3}$), this recombination time is about 10 ns, a rough upper limit for achieving equilibrium during a typical ablation pulse via this mechanism.

Region III. In Region III, also called the coronal region by analogy with solar physics, collisions are infrequent for thermal electrons and virtually nonexistent for energetic electrons. Hot electrons that developed in previous regions begin to decouple from the Maxwell–Boltzmann distribution, violating local thermodynamic equilibrium (LTE) [see Figure 4A.1; also the next subsection (*Region IV*) and Section 4A.1.5 (*Coulombic Equilibration Times...*), below]. Here, three-body recombination ceases to be a factor, except for *very* long (millisecond-duration) laser pulses.

Heating by inverse bremsstrahlung still exists (see the wavy lines in Figure 4A.1) and, although small compared to the heating rate in Region I, may counterbalance adiabatic cooling, making it difficult to estimate the variation $T_e(x)/T_{eT}$ in a universally applicable way. Boland et al. (1968) did measure $T_e(x)$ and $n_e(x)$ in a ruby laser experiment with poly(ethylene) targets at irradiance levels around $0.3\,\mathrm{TW/cm^2}$ ($3\,\mathrm{PW/m^2}$) and found

$$T_e(x)/T_e(x_T) = [n_e(x)/n_e(x_T)]^{2/3} \tag{5}$$

which is the prediction of ideal-gas adiabatic expansion theory (see Section 4A.1.6, below). Taken together, Eqs. (3) and (5) predict a $(x/x_T)^{-1.5}$ variation for the (thermal) plasma temperature.

Region IV. In Region IV, a minority population of hot electrons completely escapes the plasma plume, owing to the lack of energy-exchanging collisions while still in the experiment volume, causing a high positive potential $e\phi \gg kT_e$ to develop, which in turn accelerates a few ions that are still in the plume region to high energy. Because $e\phi \gg kT_e$, LTE no longer applies to these hot electrons [see the discussion of TE and LTE in Section 4A.1.5 (*Coulombic Equilibration Times...*) and of acceleration in Section 4A.3, below]. These hot electrons depart from the majority Maxwell–Boltzmann distribution and cease to obey the physics derived from the assumptions of LTE. Because of the strong electric field due to the separation Δx [which may be much greater than a Debye length (D_e—see Section 4A.1.5 (*The Debye Shielding Distance...*), below],

$$E = -4\pi e n_e \Delta x \qquad \text{esu/cm}$$

or

$$E = -e n_e \Delta x/\varepsilon_0 \qquad \text{V/m} \tag{6}$$

the ions rapidly reach the same average velocity as the electrons. Given a sufficiently large volume, the electron and ion clouds may actually oscillate through each other's position because of the low collision rate, at a continually decreasing plasma frequency corresponding to the decreasing electron cloud density as expansion proceeds. The plasma frequency is

$$f_p \sim \frac{\omega_p}{2\pi} = \left(\frac{n_e e^2}{\pi m_e}\right)^{1/2} = 8978(n_e^{1/2}) \qquad \text{Hz}$$

or, in SI, (7)

$$f_p = \frac{\omega_p}{2\pi} = \frac{1}{2\pi}\left(\frac{n_e e^2}{\varepsilon_0 m_e}\right)^{1/2} = 8.978(n_e^{1/2}) \qquad \text{Hz}$$

In a time-of-flight experiment where $n_e = 10^6\,\mathrm{cm}^{-3}$ ($10^{12}\,\mathrm{m}^{-3}$), plasma oscillations might be seen with a period $\tau_p = 1/f_p \approx 100\,\mathrm{ns}$.

After the interaction, the co-motional cloud of ions has nearly all the hot electrons' initial drift energy, because of the electrons' much smaller mass. Depending on Z, this energy may be distributed among a smaller number of particles (see Section 4A.3.2, below), but the drift velocity of the two velocity-decoupled clouds should ultimately be equal.

Plasma physics is normally treated by classical approximations because the quanta are normally quite small compared to, e.g., thermonuclear values of kT_e. However, it is important to realize that

$$\hbar\omega_p = 3.71 \times 10^{-11}(n_e^{1/2}) \qquad \text{eV}$$

or, in SI, (8)

$$\hbar\omega_p = 3.71 \times 10^{-14}(n_e^{1/2}) \qquad \text{eV}$$

Thus, the energy of a plasma quantum is already 1 eV when the plasma electron density is $7.2 \times 10^{20}\,\mathrm{cm}^{-3}$ ($7.2 \times 10^{26}\,\mathrm{m}^{-3}$), a density which is equal to the critical density for 1.25 μm light. Plasma quanta are on the order of 10 eV in metals where n_e is on the order of $10^{23}\,\mathrm{cm}^{-3}$ ($10^{29}\,\mathrm{m}^{-3}$). For $n(x)$ given by Eq. (3), f_p continually decreases with the expansion, nearly linearly, according to $(x/x_T)^{-10/9}$.

4A.1.3. Applicability Conditions for High-Irradiance Theory

In the heading of Section 4A.1, we picked the irradiance value $1\,\mathrm{GW/cm^2}$ to illustrate the boundary to the high-irradiance regime. This choice is a convenient oversimplification. In fact, there is no single intensity that can define the boundary. For the theory of high irradiance to clearly apply, the following four conditions must be met, at least approximately.

Condition I: Vacuum Environment. Many ablation experiments (as members of the general class in which LIMA work is found) are done in air, and in some cases the ablation depth is not too different in air or in vacuum (see, e.g., Kelly et al., 1985; and Section 4A. 2, below). Nevertheless, the underlying physics of an ablation jet in air is so much more complex than that in vacuum that simple analytical predictive capability is lost. In terms of observables, the main effect of adding more than about 1 torr of air to the problem is to *increase* target momentum coupling due to "tamping" by the air (Beverley and Walters, 1976), to decrease ablation velocity due to the "snowplow" effect, and to limit the laser irradiance that can be delivered to the target to a value equal to the air breakdown threshold irradiance (Figueira et al., 1981; Golub' et al., 1981). Further, interaction energy is devoted to the launching of so-called laser-supported detonation (LSD) waves and, for longer pulses, laser-supported combustion (LSC) waves, which can totally decouple the interaction from the original target (Beverley and Walters, 1976). This is in addition to obvious gas phase chemistry (see, e.g., Nogar, 1991; Otis and Dreyfus, 1991).

Condition II: Surface Absorber. Surface absorbers are defined (Phipps et al., 1988) as those for which the thermal penetration depth during a laser pulse of duration τ,

$$x_{\text{th}} = 0.969[(\kappa\tau)^{1/2}] \gg 1/\alpha \tag{9}$$

is much larger than the laser penetration depth. Here, $\kappa = K/\rho C$ is the thermal diffusivity of the material (units L^2/t), which among common metals ranges from 1.15 (Cu) to 0.068 cm^2/s (Bi) (Batanov et al., 1972); K is the thermal conductivity; ρ, the mass density; and C, the specific heat. This condition has also been expressed as (Kelly et al., 1985)

$$\tau_{\text{thermal}} \approx L_0^2/\kappa \ll \tau \tag{10}$$

where $L_0 = 1/\alpha$ is the laser penetration depth. In any case, the result is a problem in which the laser interaction can be modeled as a continuous plane heat source at the target surface.

"Volume absorbers" such as undoped poly(methyl methacrylate) (PMMA) at 248 nm [at low laser irradiance near plasma threshold (see Phipps et al., 1990)] show momentum coupling and other properties that increase dramatically from what is obtained for surface absorbers. One obtains momentum coupling coefficients on the order of 100 $\text{dyn}\cdot\text{s}\cdot\text{J}^{-1}$ (10^7 $\text{n}\cdot\text{s}\cdot\text{J}^{-1}$) at irradiance near the plasma threshold, rather than the 1–10 $\text{dyn}\cdot\text{s}\cdot\text{J}^{-1}$ (10^5–10^6 $\text{n}\cdot\text{s}\cdot\text{J}^{-1}$) experienced by surface absorbers.

This coupling enhancement is not yet predictable in simple closed form from just the laser irradiance I, wavelength λ, and pulse duration τ, but depends strongly on material properties such as specific heat, ionization energy, thermal conductivity, and equation of state.

As a consequence, vaporization depth x_v in volume absorbers is very material dependent and depends mainly on laser "fluence" $\Phi \equiv \int_{-\infty}^{\infty} d\tau\, I(\tau)$ (see Taylor et al., 1987). As an example of the importance of fluence, the very short pulse laser ablation work (τ = 160–300 fs) of Küper and Stuke (1989) and Srinivasan et al. (1987) shows little difference in ablation depth obtained from work done with 10^4 times longer pulse widths $\tau \approx 10$ ns at the same fluence (though the sharpness of the ablation features obtained was quite different). In this connection, see Condition IV, below.

Volume absorbers benefit from trapped ablation either through absorption at depth within the material or through deliberate imposition of a heterogeneous transparent tamping layer on top of the absorbing medium. Although their experiments were done in air rather than vacuum, and the significant "tamping" effect of air (tending also to improve coupling of the detonation) was ignored in their analysis, interesting results on the order of 700 $\text{dyn}\cdot\text{s}\cdot\text{J}^{-1}$ were obtained by Fabbro et al. (1990), using 3 and 30 ns pulses from an Nd:glass laser (1.06 μm) and $I \approx 300\ \text{MW/cm}^2$ (3 TW/m^2).

High irradiance in itself ensures the achievement of condition (9). This is because the ambient spectrophotometric absorption depth $1/\alpha_a$ is dramatically decreased by high-irradiance temperature and pressure effects, including free-electron absorption, to the point where the interaction with a target that was "volume absorbing" at low irradiance is indistinguishable in its behavior from that of a metallic target.

Condition III: Plasma Ignition. For surface absorbers in vacuum, an estimate of the onset of plasma dominance of the laser–surface interaction is given by the relationship (Berchenko et al., 1981; Phipps et al., 1988)

$$I(\tau^{1/2}) \geqslant B \tag{11}$$

where τ is the laser pulse length. Over at least a 5 orders of magnitude range in pulse duration from 1 ms to 10 ns, and laser wavelength in the range 0.25–10 μm, the constant $B_{\text{max}} \approx 8 \times 10^4\ \text{W}\cdot\text{s}^{1/2}\cdot\text{cm}^{-2}$ ($8 \times 10^8\ \text{W}\cdot\text{s}^{1/2}\cdot\text{m}^{-2}$) when plasma dominates the interaction. The plasma formation threshold occurs at $B_p \approx \frac{1}{2}B_{\text{max}} = 4 \times 10^4\ \text{W}\cdot\text{s}^{1/2}\cdot\text{cm}^{-2}$ ($4 \times 10^8\ \text{W}\cdot\text{s}^{1/2}\cdot\text{m}^{-2}$). This point is illustrated in Figure 4A.2.

This value for B_p is accurate within a factor of 2 for most metals in vacuum. It is also a good upper limit value for dielectrics but can be lower in the presence of strongly absorbing surfaces (Phipps et al., 1990). For very

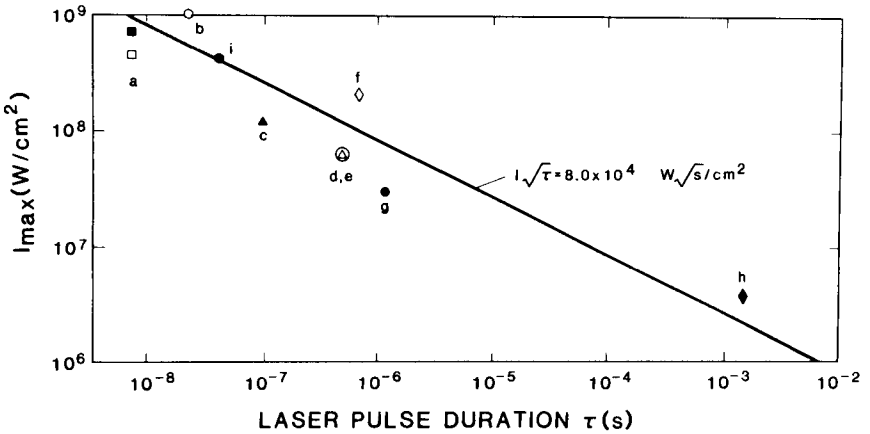

Figure 4A.2. A survey of intensities for plasma dominance of the laser–surface interaction in vacuum on metals at several wavelengths from Phipps et al. (1988), used by permission: (a) Gregg and Thomas (1966a,b), $\lambda = 694$ nm, $\tau = 7.5$ ns, Be; (b) Phipps et al. (1988), $\lambda = 248$ nm, $\tau = 22$ ns, Al; (c) Ursu et al. (1981), $\lambda = 10.6\,\mu$m, $\tau = 100$ ns, stainless steel; (d) Rosen et al. (1982b), $\lambda = 350$ nm, $\tau = 500$ ns, Ti alloy; (e) Rosen et al. (1982a), $\lambda = 350$ nm, $\tau = 500$ ns, Al alloy; (f) Phipps et al. (1988), $\lambda = 10.6\,\mu$m, $\tau = 700$ ns, Al; (g) Duzy et al. (1980), $\lambda = 350$ nm, $\tau = 1.2\,\mu$s, Al; (h) Afanas'ev et al. (1969), $\lambda = 1.06\,\mu$m, $\tau = 1.5$ ms, Al; and (i) Phipps et al. (1988), $\lambda = 248$ nm, $\tau = 37$ ns, Al.

short pulses and transparent materials, B is somewhat larger. For pulses in the range 10 ps–10 ns and for transparent dielectrics such as NaCl, B_p increases to about $5B_{max}$ (see Smith, 1978). Further details of plasma ignition are discussed below in Section 4A.1.4.

Condition IV: Laser Pulse Not Too Short. For high-irradiance scaling theory to predict the depth, x_v, of material removed as well as it does the impulse, we have one more requirement: the duration of the pressure pulse on the target surface must be of the same order as or smaller than the laser pulse duration. In high-irradiance laser irradiation experiments, this condition is normally considered to be satisfied. Quantitatively, the condition is satisfied if the laser-absorption region near the target surface is able to expand much farther than the standoff distance x_I [see Section 4A.1.6 (*Adiabatic Expansion Theory*...), below], allowing the surface pressure to drop substantially after the laser pulse ceases, in a time much shorter than the laser pulse. In other words, a validity limit for our theory is

$$\tau \gg t_I = x_I/v_a \qquad \text{s} \tag{12}$$

where the velocity of the absorption front, v_a, is approximately equal to c_s

for purposes of comparison. Note that the standoff distance x_I is not necessarily equal to the flow transition distance x_T.

To understand this limitation, we need to compute x_I and t_I. We will do this later [in Section 4A.1.6 (*Adiabatic Expansion Theory*...)], after development of additional concepts. Here, we will simply state the result:

$$t_I = 8.6 \times 10^{-5} A^{7/8} I^{1/2} \lambda^{3/2} \tau^{3/4} \qquad \text{s}$$

or, in *SI*,

$$t_I = 8.6 \times 10^{-4} A^{7/8} I^{1/2} \lambda^{3/2} \tau^{3/4} \qquad \text{s} \tag{13}$$

For example, for 10 ns KrF experiments on a silicon target ($A = 28$) at 10 GW/cm^2 (100 TW/m^2) irradiance, the theory should predict impulse well, because $t_I = 20$ ps. For a 10 ns, 10 μm laser, the same conditions would require $\tau \gg 5$ ns, so that the prediction might not be as good. As a third example, with $I = 10$ PW/cm^2 (10^{20} W/m^2), $\lambda = 248$ nm, $\tau = 1$ ps, and $A = 63.5$ (copper), we find $t_I = 40$ ps, and $\tau \gg t_I$ is clearly not satisfied.

For pulses of picosecond and shorter duration, special considerations such as shock heating come into play and for example, very-high-irradiance 100 fs ablation experiments will not be modeled by our theory [see Section 4A.1.6 (*Adiabatic Expansion Theory*...).

4A.1.4. High-Irradiance Absorption and Ignition at the Solid Surface

Under most experimental conditions, awaiting the few initial electrons does not appear to be a hindrance to breakdown. The first few electrons are probably present owing to one or more of the following phenomena:

- Multiphoton ionization of atomic or molecular species in the plume
- Penning ionization from excited states in the plume
- Fracture ejection of ions and electrons from the surface
- Thermionic emission from hot surfaces (including those of ejected particulates), usually at temperatures >1000 K, even for polymers; we will emphasize this mechanism

While the last-named mechanism could supply large currents, space charge effects over the surface choke off the supply of electrons at a flux about 10^9 cm^{-2}, as charge-compensating ions are not present.

If these electron sources were not present, then ablation-plasma thresholds would be in the 100 GW/cm^2 region, instead of 1 GW/cm^2.

In the general case, after vapor is present, the physical mechanisms that produce plasma are either collisional ionization or photoionization, depending

on the ratio of incident photon energy to the atomic energy levels available in the vapor (Raizer, 1977).

Initiation. The functional form of Eq. (11) results from analysis of uniform-rate heating of a semi-infinite slab, where the heated layer thickness is given by (see Carslow and Jaeger, 1959)

$$x_{th} = 0.969[(\kappa\tau)^{1/2}] \tag{14}$$

The resulting surface temperature is

$$\Delta T = \frac{2I_{abs}(\tau^{1/2})}{(\pi K\rho C)^{1/2}} \tag{15}$$

In Eqs. (14) and (15), I_{abs} is the absorbed irradiance; K, the thermal conductivity; C, the specific heat; and $\kappa = K/\rho C$, the thermal diffusivity.

In the simplest analysis, the temperature of the irradiated solid surface rises until the vapor pressure above the surface is sufficient for the laser irradiance to cause plasma formation. Even if the surface absorptivity I_{abs}/I is known, the microscopic state of the surface may depress the ignition threshold below what would be predicted by Eq. (10). See, for example, the insulated surface defect model of Glickler et al. (1980), which supposes that microscopic flakes on the material surface ignite plasma in the vapor via thermionic emission. The particle current density for the thermionic emission is given by the Richardson–Dushman equation ($e\phi_w$ is the surface work function energy (Coles, 1976):

$$\Gamma_e = \frac{4\pi m_e(kT)^2}{h^3}\exp(-e\phi_w/kT) \qquad e\cdot s^{-1}\cdot cm^{-2} \tag{16}$$

Collisional Breakdown. In the infrared (IR), e.g., with CO_2 lasers, the mechanism for initial plasma formation is (collisional) ac avalanche breakdown in the target vapor. The small initial background density of electrons is accelerated by the electric field of the laser light, repeatedly colliding with neutral atoms until some of them reach their ionization threshold. This mechanism is inverse bremsstrahlung heating. With I in W/cm^2 (W/m^2) and E in V/cm (V/m), the magnitude of the electric field of the light wave is

$$E = 27(I^{1/2}) \tag{17}$$

With sufficient dephasing collisions per optical cycle, this field is available for electron acceleration. As an example, the available accelerating field is

27 MV/cm at 1 TW/cm^2 (10 PW/m^2) irradiance. With sufficient irradiance and time, this process exponentiates as the collision frequency increases with ionization density, until complete ionization occurs. Avalanche ionization can be quite efficient and rapid. Even if $\hbar\omega = 117$ meV and $E_I/\hbar\omega \approx 100$, as with CO_2 laser-induced ionization, the critical density $n_{ec} = 9.9 \times 10^{18}$ cm^{-3} can be reached in picoseconds through this mechanism, starting from perhaps $n_{e0} = 10^3$ cm^{-3}. Enough atoms are available in air at 150 torr to create n_{ec} with full ionization. This process is particularly efficient in the IR, as collision and laser frequencies are similar in magnitude.

The (collision-dominated) IR optical intensity breakdown threshold for neutral gases is inversely proportional to vapor pressure up to several atmospheres (see Gill and Dougal, 1965; Grey Morgan, 1978). Therefore, above a certain threshold laser intensity, laser vaporization simply increases the pressure at the surface until the breakdown threshold is achieved.

Photoionizaton. On the other hand, for ultraviolet (UV) wavelengths, direct photoionization of the vapor atoms is often the predominant ionization mechanism. For example, the photon energy $\hbar\omega = 5$ eV of KrF is sufficient to photoionize many metal vapors via two or three steps involving low-energy, intermediate excited states [e.g., titanium (see Rosen et al., 1982a, and associated references) and copper (see Dreyfus, 1991)].

Between these extremes of wavelength, one might expect that the dominant ionization mechanism during the laser pulse would depend on the atomic physics of the target material. After the initial formation stage, direct photoionization can play an important role with IR laser irradiation as well, since a dense plasma, once formed, is an efficient IR-to-UV converter. This is because one is dealing with a hot-electron gas. Since the peak of the blackbody spectrum (per unit frequency interval) is given by

$$T\lambda_{max} = 440 \qquad nm\cdot eV \tag{18}$$

an optically thick hot-electron gas radiates a principal color that is well into the hard UV for the expected temperature at $\geqslant 2$ eV.

Collisionless Ionization. Multiphoton, collisionless, photoionization is a very-high-irradiance, low-pressure phenomenon. One necessary precondition is (Grey Morgan, 1978)

$$(p\tau)_{mp} < 1 \times 10^{-7} \qquad torr\cdot s$$

or, in SI, (19)

$$(p\tau)_{mp} < 1.33 \times 10^{-5} \qquad Pa\cdot s$$

The other is adequate optical electric field to actually strip electrons off individual atoms without collisions. The transition probability for the process is

$$\mathbf{P} = C_i \omega \tau N_{\min}^{2/3} \left[\frac{W_{osc}}{2W_i} \right]^{N_{\min}} \tag{20}$$

(see Johann et al., 1986), where $\mathbf{P}$ is the probability (per atom); τ is the laser pulse width; $C_i \approx 1$; W_i is the ionization potential of the atom; $N_{\min}$ is the minimum number of laser photons of energy $\hbar\omega$ sufficient to overcome the modified ionization threshold $W_i(I) = W_i + W_{osc}$; and W_{osc} is the "quiver energy" of an electron in the laser field,

$$W_{osc} = eE^2/4m\omega^2 = 8.4 \times 10^{-13} I \quad \text{eV} \tag{21}$$

with I in W/cm^2 (the coefficient is 8.4×10^{-17} for I in W/m^2 to yield eV).

In other words,

$$N_{\min} = [W_i + W_{osc}]/\hbar\omega \tag{22}$$

As an example, for argon at 0.2 torr, subjected to a 50 ns, 3 μm IR laser, the collisionless ionization threshold is about 25 TW/cm^2, and $N_{\min} = 89$. The conditions $n_0\mathbf{P} = 10^{10}\,\text{cm}^{-3}$ can be used as the ionization threshold.

At vapor pressures above about 0.2 torr (27 Pa), collisional processes will come into play at lower irradiance levels than collisionless ones. Therefore, we expect this mechanism to have small importance for most LIMA work, considering the very high irradiance and low pressure required for it to be the dominant source of ionization.

Saha Equilibrium. Exact ignition scenarios must be calculated using a specific computer model that takes detailed account of material properties and laser parameters (see, e.g., Vertes et al., 1989). However, a good understanding of the relation between temperature and ionization density in LTE can be obtained from the simplified Saha equation (see Vertes and Juhasz, 1989):

$$\frac{\eta^2}{1-\eta} = \frac{1}{n_\Sigma}\left(\frac{2\pi m_e k T_e}{h^2}\right)^{3/2} \exp(-W_i/kT_e) \tag{23}$$

In this expression, W_i is the first ionization potential of the neutral vapor; T_e, the electron temperature; $n_\Sigma = n_0 + n_e$ (cm^{-3}), the total number density; and $\eta = n_e/n_\Sigma$, the ionization fraction obtained. It should be pointed out that,

in the high-irradiance cases we consider in this section, we have $\eta \to 1$ early in the laser pulse, the precise value of η being unimportant.

4A.1.5. Absorption and Energy Redistribution Processes in Dense LTE Plasma

Local Thermodynamic Equilibrium (LTE). Most systems never achieve complete thermodynamic equilibrium (TE). Although the departure may be small, a system to which a pulse of energy is added or subtracted is, at least momentarily, out of TE. Equilibria exist that are not thermal equilibria. Collisions and collision-like particle-field damping processes restore TE. Because relaxation time increases with increasing size of a system, separate small parts of a system will reach a state of internal equilibrium long before they equilibrate with each other (see Landau and Lifschitz, (1958). Therefore, TE is first restored locally, hence LTE.

In electrolytes, these times are very fast because the density is high, and departures from TE in chemistry are often short-lived. In plasmas, equilibration times can be short enough, in some experimental conditions, for energetic particles to escape the experiment before TE is achieved.

Coulombic Equilibration Times and Mean Free Paths. For temperatures of a few electron volts and modest densities one would expect that, in Regions III or IV (see Figure 4A.1), dephasing collisions that produce LTE are dominated by coulombic interactions among the plasma particles. Since these are of quite different mass—in an electron–ion plasma, $m_i/m_e = 1836A$, where A is the atomic mass number—separate LTEs for each set of particles may coexist for a time because of the coulombic equilibration-time hierarchy (Montgomery and Tidman, 1964):

$$\tau\left[\begin{matrix}\text{electrons become}\\ \text{isotropic and}\\ \text{Maxwellian}\end{matrix}\right] : \tau\left[\begin{matrix}\text{ions become}\\ \text{isotropic and}\\ \text{Maxwellian}\end{matrix}\right] : \tau\left[\begin{matrix}\text{electrons \& ions}\\ \text{reach}\\ \text{equilibrium}\end{matrix}\right]$$

$$= \left(\frac{m_e}{m_i}\right) : \left(\frac{m_e}{m_i}\right)^{1/2} : 1 \tag{24}$$

$$= \frac{1}{1836A} : \frac{1}{(1836A)^{1/2}} : 1$$

As an example, for copper, these times are in the ratio 10^5:300:1. The electrons reach LTE quite rapidly because of their high thermal velocity, whereas the ions do so more slowly owing to their smaller velocity and higher mass, Because at most m_e/m_i values the kinetic energy can be transferred in an

inefficient electron–ion collision, the population of electrons take still longer to share energy with the ion population.

The expression for the coulombic electron–ion energy exchange time is (Spitzer and Härm, 1958)

$$\tau_{eiE} = \frac{2^{5/2} A m_p (kT_e)^{3/2}}{\pi^{3/2} (m_e)^{1/2} Z n_e e^4 \ln\Lambda} \tag{25}$$

while the corresponding expression for the mean free path (MFP) for electron–ion energy exchange is

$$\lambda_{eiE} = v_{the}\tau_{eiE} = \frac{2^{5/2}}{\pi^{3/2}} \frac{A m_p}{m_e} \frac{(kT_e)^2}{Z n_e e^4 \ln\Lambda}$$
$$\approx 10^8 A T_e^2 / Z n_e \quad \text{cm} \tag{26}$$

taking $\ln\Lambda = 7$. The quantity Λ is defined in a later subsection [see Eq. (31)]. The coefficient in Eq. (26) becomes 10^{12}, rather than 10^8, when SI units are used. The quantity $v_{the} = (kT_e/m_e)^{1/2}$ is the electron thermal velocity (rigorously, the speed corresponding to the most probable kinetic energy in a Maxwellian velocity distribution).

Physically, the form of Eq. (26) reflects the fact that the cross section σ_{sc} for coulombic scattering of an electron by an ion is inversely proportional to the fourth power of electron velocity and thus the second power of electron temperature (see, e.g., Spitzer, 1967), so that a coulombic MFP has the dependence $\lambda_{eiE} = 1/(n_e\sigma_{sc}) \propto T_e^2/n_e$ on density and temperature.

Figures 4A.3 and 4A.4 show a calculation of the MFP for electrons in energy exchange, $\lambda_{eiE} = v_{the}\tau_{eiE}$, for a Maxwellian plasma formed from copper vapor, and of τ_{eiE}, respectively, with three-body recombination effects (see the following subsection) included. It is seen that the electron MFP for energy loss, even for a temperature of 1 eV, exceeds the size of a typical experiment when $n_e(x)$ has dropped to $10^{16}\,\text{cm}^{-3}$. This situation, which can occur in a Region II thickness as small as 300 μm in a KrF experiment with target spot size $d_s = 1$ μm, is the definition of Region III. For a typical initial laser-induced plasma expansion velocity (in Region I) of 10 μm/ns, the plasma can expand into Region III within 30 ns.

Effects of Three-Body Recombination on Equilibration. Most of the electron–ion relaxation times in Table 4A.2 are quite long. However, for low temperatures and high densities such as one expects in Region I or II (see Figure 4A.1), three-body recombination may dominate coulombic interactions. Three-body recombination and its inverse, collisional ionization, must take

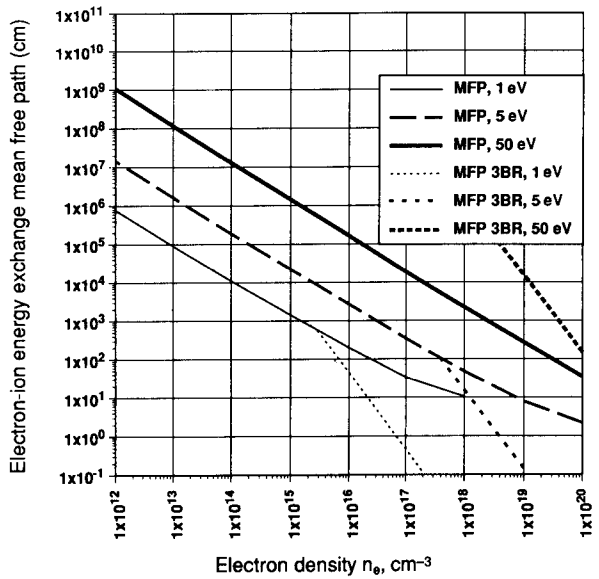

Figure 4A.3. Graph showing the mean free paths λ_{eiE} and λ_{ei3BR} (electrons on cold ions) for copper with $Z = 1$ vs. electron density for three electron temperatures.

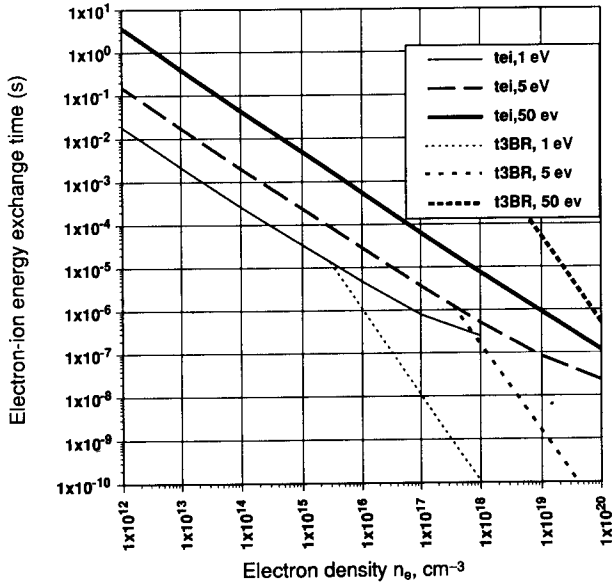

Figure 4A.4. The energy exchange times τ_{eiE} and τ_{ei3BR} (electrons on cold ions) for copper with $Z = 1$ vs. electron density for three electron temperatures.

Table 4A.2. Illustrative Values for Singly Ionized Copper Plasma

Region	n_e (cm^{-3})	T_e (eV)	T_e (K)	D_e	f_p	$\Lambda = n_e D_e^3$	τ_{ee}	τ_{ii}	τ_{ei}	τ_{ei3BR}
I ($\lambda = 1\,\mu m$, IB absorption zone)	10^{21}	3	3.48×10^4	4.1 Å	284 THz	0.28	—[a]	—[a]	—[a]	16 fs
II (mid-expansion near target)	10^{18}	5	5.80×10^4	17 nm	9 THz	19	4.4 ps	1.5 ns	520 ns	160 ns
III (mid-corona, hot electrons)	10^{14}	10	1.17×10^5	2.4 μm	90 GHz	5.4×10^3	43 ns	15 μs	5 ms	0.5 yr
IV (ion beam, hot electrons)	10^8	50	5.80×10^5	5.3 mm	90 MHz	6.1×10^7	230 ms	79 s	7.5 h	16 Gyr
Interstellar gas	1	1	1.16×10^4	740 cm	9 kHz	1.7×10^9	15 h	220 days	200 yr	3.6×10^{18} yr
Stellar interior	10^{24}	2000	2.32×10^7	3.3 Å	9 PHz	150	21 fs	7.1 ps	2.4 ns	80 ns

[a]Concept not valid because $\Lambda \neq \gg 1$.

place at equal rates in LTE:

$$2e + n_i(Z+1) \leftrightarrow n_i(Z) + e \tag{27}$$

It is a nonradiative process.

When conditions are appropriate in laser–plasma interactions, three-body recombination becomes dominant very rapidly, since it depends on the square of the electron density and the 4.5 power of temperature (see, e.g., Book, 1989):

$$\tau_{ei3BR} = 5.85 \times 10^7 T_e^{4.5}/n_e^2 \tag{28}$$

The corresponding electron MFP has an even stronger temperature dependence:

$$\lambda_{ei3BR} = v_{the}\tau_{ei3BR} = 2.28 \times 10^{13} T_e^5/n_e^2 \quad \text{cm} \tag{29}$$

[for SI units, the correct prefatory constant in Eq. (28) is 5.85×10^{19}, and in Eq. (29) is 2.28×10^{23} to yield MFP in meters].

The decay of both τ_{ei3BR} and τ_{eiE} with distance can be quite rapid, depending sensitively on the actual evolution of the plasma temperature during the expansion. For example, if the density varies with distance from the target according to $(x/x_T)^{-2.5}$ [see Eq. (4)] while the temperature stays constant, the recombination time τ_{ei3BR} varies at least as rapidly as

$$\tau_{ei3BR} \propto (x/x_T)^{-5} \tag{30}$$

while the coulombic τ_{eiE} for the thermal plasma, under the same conditions, varies only as $(x/x_T)^{-1}$. Using electron density and temperature implied by 1 GW/cm^2 of 248 nm radiation striking a Cu target for 10 ns, one estimates an ablation flux of 2.2×10^{18} $Cu^0\,cm^{-2}$ and 3×10^{17} $Cu^+\,cm^{-2}$ (see Vertes and Juhasz, 1989). For the sake of discussion, let us take the distribution of ion expansion velocity to be a "top hat" extending from 1.5 to 3 cm/μs, i.e., from one to two times the Boltzmann velocity, and the laser spot diameter on target to be 1 mm. Because the Cu^+ density is about $2 \times 10^{19}\,cm^{-3}$, three-body recombination is extremely rapid during the 10 ns ablation pulse ($\tau_{ei3BR} \approx 20$ ps), while the ablation front achieves a thickness of about 200 μm.

The success of models based on LTE, especially for short times and expansion distances, is explained by the fact that collisional processes can be so rapid near the target.

Assuming an expansion cone angle $\theta_d = 24°$, we have $x_T = 3.7$ mm. We take the initial electron temperature under these conditions to be 2.6 eV,

based on the work of von Gutfeld and Dreyfus (1989). Applying Eq. (28) to this experiment, we find that τ_{ei3BR} will have increased from 20 ps to 10 ns in a drift distance $x = 4x_T = 1.5$ cm ($\tau \approx 0.7\,\mu$s) and to 10 μs in $x \approx 7$ cm ($\tau \approx 3.5\,\mu$s). Meanwhile, the coulombic τ_{eiE} in the thermal plasma will have increased from 750 ns to 10 μs, so that coulombic processes will begin dominating three-body processes, insofar as equilibration between the electron and ion populations is concerned, only after expansion has proceeded 7 cm from the target. Note that the dominant collisional processes act to rapidly equilibrate the low-velocity component of the particle velocity distributions, which then equilibrate within themselves much more rapidly than τ_{eiE} [by the factors given by Eq. (24)].

Now, let us consider a LIMA-type ablation, in which the laser spot on target is as small as 10 μm in diameter. With a cone angle $\theta_d = 24°$, we have $x_T \approx 40\,\mu$m, a distance that can be attained by the plume at 2 cm/μs in ≈ 2 ns, well before the laser pulse ends. Again, $\tau_{ei3BR} \approx 20$ ps, whereas $\tau_{eiE} \approx 750$ ns. Here, the crossover to dominance by coulombic interactions occurs much sooner because of the smaller scale. Applying Eq. (28) to this experiment, we find that τ_{ei3BR} will have increased from 20 ps to 10 ns in a drift distance $x = 160\,\mu$m ($\tau \approx 8$ ns), and to 10 μs in $x \approx 0.8$ mm ($\tau \approx 40$ ns). Coulombic processes will become more important than three-body processes after expansion has proceeded 0.8 mm from the target, although they will still be as infrequent as before and, when dominant, support the generation of hot electrons.

Choosing $\sigma_{3BR} = 3$ Å^2 as a typical recombination cross section, we see that at a density 1×10^{19} cm^{-3}, the ion MFP for recombination $1/(n\sigma_{3BR}) = 3\,\mu$m, a significant fraction of the ablation region radius in this case. This may explain why diatomics are commonly dissociated with large (1 mm diameter) ablations whereas they often survive the plasma in a 10 μm diameter interaction.

Experimentally, the lack of communication back to the slower neutrals has been observed, in the sense that it is the faster diatomics that are dissociated. The more intense the plasma, the fewer energetic diatomic species are observed (see Dreyfus et al., 1986c; Pappas et al., 1992).

The Debye Shielding Distance and Debye Sphere. The quantity Λ is the number of particles in a Debye sphere,

$$\Lambda = \frac{4\pi}{3} n_e D_e^3 \tag{31}$$

The electron Debye length, D_e, is the distance within which ion charge fluctuations cannot be neutralized by electron motions. The significance of Λ is that, if $\Lambda \neq \gg 1$, the plasma may no longer be regarded as a gas, and the Boltzmann distribution is inapplicable; D_e and Λ are among the most important LTE concepts in plasma physics.

The Debye–Hückel theory, originally developed to treat charge motion in electrolytes, also describes a plasma with a distribution of electrons in thermal equilibrium. Their spacial density will then be given by the Boltzmann factor $\exp(-e\phi/kT)$, where $\phi(r)$ is the electrical potential, or

$$n_e(r) = n_0 e^{-e\phi/kT} \tag{32}$$

If now a single test ion Ze is placed at the origin in this distribution of electrons (assuming charge neutrality, but considering the other ions to be a smeared-out, positive-charge background), Poisson's equation is

$$\begin{aligned} \nabla^2\phi &= -4\pi e\{Z\delta(r) - n_0[e^{-(e\phi/kT} - 1]\} \\ &\approx -4\pi e\{Z\delta(r) + en_0\phi/kT\} \end{aligned} \tag{33}$$

with the linearizing approximation $e\phi \ll kT$. The solution to Eq. (33) is

$$\phi = \phi_0 \exp(-r/D_e) \tag{34}$$

where $\phi_0 = e/r$ ($e/4\pi\varepsilon_0 r$ in SI) is the electric potential of a single ion. The Debye length, D_e, in a plasma depends on electron density, n_e, and temperature, T_e, according to

$$D_e = \frac{v_{the}}{\omega_p} = \left(\frac{kT_e}{4\pi n_e e^2}\right)^{1/2} = 6.9\left[\left(\frac{T_e}{n_e}\right)^{1/2}\right] \quad \text{cm} \tag{35a}$$

or

$$D_e = \frac{v_{the}}{\omega_p} = \left(\frac{\varepsilon_0 kT_e}{n_e e^2}\right)^{1/2} = 69\left[\left(\frac{T_e}{n_e}\right)^{1/2}\right] \quad \text{m} \tag{35b}$$

Table 4A.2 gives Debye lengths from Eq. (35), electron plasma frequencies from Eq. (7), and the times τ_{ee}, τ_{ii}, and τ_{ei} from Eq. (25) for typical densities and temperatures illustrative of the regions of Figure 4A.1 and for other conditions. Note that, if the ions are *not* assumed to be a smeared-out positive-charge background, but rather discrete point sources, one gets a coefficient $(1/8\pi)^{1/2}$ vs. $(1/4\pi)^{1/2}$ in Eq. (35a) (see Ginzburg, 1970). However, the convention is as stated in Eq. (35a,b). Normally D_e is much smaller than the plume thickness for nanosecond laser ablation work; hence electric and magnetic fields do not penetrate the plume except in the outermost coronal region.

Ambipolar Diffusion and Debye Sheaths. In this section, we assume that the Debye length D_e is less than d_s, the diameter of the laser interaction region. Free rather than ambipolar diffusion occurs in the unusual event that this condition is violated (Weyl, 1989). In LIMA work, such a violation would occur for laser spot sizes on the order of 1 Å (see Section 4A.3), an extremely unlikely occurrence.

Where Γ is the particle current (units: $L^{-2}\cdot s^{-1}$), the electron and ion particle current equations are

$$\Gamma_e = -\mathscr{D}_e \nabla n_e - \mu_e E n_e$$

and (36)

$$\Gamma_i = -\mathscr{D}_i \nabla n_i + \mu_i E n_i$$

The mobility μ_i of species j is given by its collision time $\tau_j = \tau_{jkp}$ for momentum exchange on the other species:

$$\mu_j = e\tau_j/m_j \tag{37}$$

and the diffusion coefficient is

$$\mathscr{D}_j = (kT/e)\mu_j \tag{38}$$

in the absence of magnetic fields (see Rose and Clark, 1961).

We take

$$n_e = Z n_i$$

and (39)

$$\Gamma_e = Z\Gamma_i$$

assuming charge neutrality. When both species flow freely, limited only by self-generated fields, an electric field will develop,

$$E = \frac{(\mathscr{D}_i - \mathscr{D}_e)\nabla n_i}{(\mu_i + \mu_e)n_i} \tag{40}$$

in a so-called sheath of thickness about equal to D_e. However, since $\mathscr{D}_e \gg \mathscr{D}_j$ and $\mu_e \gg \mu_i$, we find

$$-eE/kT_e \approx \nabla n_e/n_e \tag{41}$$

The electric field E can be very large. Eliezer and Hora (1989) predict values

on the order of 100 MV/cm (10 GV/m) for the plasma electric field generated by 0.5 ps Nd:glass laser irradiation at 10 PW/cm^2 (10^{20} W/m^2).

However, under LTE, the *distance* over which such a field exists is correspondingly small. What normally happens in response to this field is the immediate formation of a so-called double layer (Hora et al., 1989), composed of just enough charge separation dipole moment

$$en_e \Delta x = -E/4\pi = eD_e^2 \nabla n_e \tag{42}$$

to balance this field and prevent the flow of current. For $n(x)$ given by Eq. (3), the density gradient scale length in the laser absorption region,

$$L_n = |n_e/\nabla n_e| = 0.45x \tag{43}$$

is on the order of 0.1 μm in typical KrF laser ablation experiments.

Thus,

$$(\Delta x/D_e) = D_e/L_n \tag{44}$$

depends on the ratio of the Debye length to the density gradient scale length and is very small near the absorption layer, where D_e is itself on the order of angstroms. If $n(x)$ is given by Eq. (3), then (near the absorption layer $x = x_I$), $\Delta x/D_e = D_e/L_n = 2.22D_e/x_I = 0.01$, for the conditions of typical KrF ablation experiments ($I = 10$ GW/cm^2, $\tau = 10$ ns, $\lambda = 248$ nm, $A = 28$, and $Z = 1$). This means that, under LTE conditions, a large field operates over a small distance, and the product

$$e\phi = E\,\Delta x = (D_e/L_n)^2 kT_e \tag{45}$$

is approximately equal to $10^{-4}\,kT_e$ at the absorption layer, small enough to be insignificant.

Of course, at extremely high irradiance levels sufficient to develop plasma ponderomotive forces, density gradient steepening by the light pressure can drastically reduce L_n, creating larger potentials than this. At irradiance levels above 10–100 TW/cm^2 (100–1000 PW/m^2), suitable for laser fusion, a copious suprathermal "hot" electron flux is generated. These electrons can bounce off the sheath repeatedly to give extra energy to ions that do escape the DL (Hauer et al., 1989). We shall return to the subject of charge acceleration in Section 4A.3.

The Plasma Dielectric Function. Defining

$$\tilde{n} = n + i\chi \tag{46}$$

for the plasma complex refractive index and

$$\varepsilon = \tilde{n}^2 = (n^2 - \chi^2) + i2n\chi \tag{47}$$

as the plasma complex dielectric function, the real (refractive) and imaginary (absorptive) parts of the dielectric constant, ε, of a nonmagnetized plasma are given by

$$\mathrm{Re}(\varepsilon) = n^2 - \frac{\omega_p^2}{\omega^2(1 + \nu^2/\omega^2)} \tag{48}$$

and

$$\mathrm{Im}(\varepsilon) = \frac{\nu}{\omega}\left[\frac{\omega_p^2}{\omega^2(1 + \nu^2/\omega^2)}\right] \tag{49}$$

so that the optical absorption coefficient is

$$\alpha = \frac{2\omega}{c}\chi = \frac{\nu}{nc}\left[\frac{\omega^2{}_p}{\omega^2(1 + \nu^2/\omega^2)}\right] \tag{50}$$

The damping frequency, ν, is provided by long-distance collision-like electron–ion coulombic, momentum-exchanging interactions in the plasma,

$$\begin{aligned} \nu = \nu_{eip} &= 1/\tau_{eip} \\ &= 7.49 Z n_e / T_e^{3/2} \qquad \text{Hz} \end{aligned} \tag{51}$$

in cgs units. For SI, the coefficient is 7.49×10^{-6} in Eq. (51). The parameter τ_{eip} is the time for electron–ion momentum exchange. Although ν_{ei} is often large in the visible and UV range, it is also often smaller than the laser frequency itself. Then, in the limits $\nu_{ei}/\omega \ll 1$, and $n \approx 1$ (valid for vacuum propagation), we have—

absorption coefficient:

$$\alpha \cong (\nu_{ei}/c)(n_e/n_{ec}) \tag{52}$$

optical cross section:

$$\sigma_{opt} \equiv \alpha/n_e \cong [\nu_{ei}/(cn_{ec})] \tag{53}$$

and

$$\varepsilon \approx n^2 \approx [1 - n_e/n_{ec}] \tag{54}$$

Inverse Bremsstrahlung Absorption and Related Terms. Inverse bremsstrahlung is so named because it is physically the inverse of the process by which electron collisions with ions generate radiation in a plasma. The quantum mechanically correct formula for the inverse bremsstrahlung absorption coefficient in a plasma where LTE applies is (Kidder, 1971)

$$\alpha = \frac{4}{3}\left(\frac{2\pi}{3kT_e}\right)^{1/2}(2\pi)^3 Z^2 n_e n_i g_{ff}\, e^6 \frac{[1 - \exp(-\hbar\omega/kT_e)]}{hcm_e^{3/2}\omega^3} \qquad \text{cm}^{-1}$$

or, with SI quantities, (55)

$$\alpha = \frac{2\pi}{3 \times 10^{23}}\left(\frac{2\pi}{3kT_e}\right)^{1/2}(2\pi)^3 Z^2 n_e n_i g_{ff}\, e^6 c^5 \frac{[1 - \exp(-\hbar\omega/kT_e)]}{hm_e^{3/2}\omega^3} \qquad \text{m}^{-1}$$

Here, $Z = n_e/n_i$ is the average ion charge state, assuming charge neutrality. The Gaunt factor, g_{ff}, is a quantum mechanical correction with magnitude very close to unity for most laser–plasma interactions (see Gaunt, 1930). In the case of longer wavelengths, e.g., radio wavelengths in the ionosphere, g_{ff} is related to the so-called Coulomb logarithm by

$$g_{ff} = (\sqrt{3}/\pi)\ln\Lambda \tag{56}$$

(see Allen, 1973; Spitzer, 1967). The quantity Λ was defined in Eq. (31).

It should be noted that this formula (55) treats electromagnetic-wave heating of plasma by assuming electron dephasing is produced exclusively by long-range coulombic interactions with ions. Electron-neutral collisions can also be important as a source of dephasing for partially ionized plasmas, but we use the full ionization approximation.

The expression $[1 - \exp(-\hbar\omega/kT_e)]$ in Eq. (55) may be taken as approximately equal to $\hbar\omega/kT_e$ for $\geqslant 5$eV plasmas and IR or visible lasers. These simplifications produce the familiar formula laser absorption:

$$\alpha = 1.97 \times 10^{-23} Z^3 n_i^2 \lambda^2 / T_e^{3/2} \qquad \text{cm}^{-1}$$

or, in SI, (57)

$$\alpha = 1.97 \times 10^{-29} Z^3 n_i^2 \lambda^2 / T_e^{3/2} \qquad \text{m}^{-1}$$

The optical absorption cross section $\sigma = \alpha/n_e$ for a plasma electron can be many orders of magnitude larger than its geometrical size πr_e^2, as can be seen by reexpressing Eq. (57) in the form

$$\sigma_{opt} = 250\left(\frac{Zn_e\lambda^2}{T_e^{3/2}}\right)r_e^2 \qquad \text{cm}^2 \tag{58a}$$

or, in SI,

$$\sigma_{\text{opt}} = 2.50\left(\frac{Zn_e\lambda^2}{T_e^{3/2}}\right)r_e^2 \qquad \text{m}^2 \tag{58b}$$

For example, if $\lambda = 10.6\,\mu$m, $T_e = 11{,}605$ K (1 eV), $n_e = 10^{19}\,\text{cm}^{-3}$, and $Z = 1$, then $\sigma_{\text{opt}} = 2.25 \times 19^9\, r_e^2 = 1.8 \times 10^{-16}\,\text{cm}^2$. A plasma with these parameters has an absorption length for 10.6 μm light given by $1/\alpha = 5\,\mu$m and is 99.9% opaque in 40 μm thickness. The functional form of Eqs. (57) and (58a,b) was predicted by the preceding analysis of the plasma dielectric function, Eqs. (52) and (53).

These equations describe a laser-produced plasma after its creation. If $n_e = 10^{19}\,\text{cm}^{-3}$, as in the preceding example, and $T_e = 3$ eV, the plasma energy density $w_p = n_e k T_e = 4.8\,\text{J/cm}^3$ (4.8 MJ/m^3). It should be kept in mind that the more one retreats toward the plasma formation threshold irradiance value, the more important become the conditions *during* the plasma creation, when this energy was deposited. At threshold irradiance, it becomes important that photon–plasma coupling mechanisms other than inverse bremsstrahlung were necessary early in the laser pulse to deposit this energy density w_p. Such processes include local density fluctuations that enhance ν_{ei}, and three-body recombination when $n_i > 10^{18}\,\text{cm}^{-3}$.

4A.1.6. What Can Be Learned About Ablation Parameters from a General Theory?

Analysis of high-irradiance ($I \geqslant 10^{11}$ W/cm^2), short-pulse ($\tau \sim 10$ ns) surface ablation has existed for years. In this section, we will show that the resulting dense ($> 10^{19}\,\text{cm}^{-3}$), thin ($\geqslant 30\,\mu$m) surface plasma can be described down to a low-power limit ($\sim 10^9$ W/cm^2 for UV) determined primarily by the inelastic scattering cross section of plasma electrons, i.e., inverse bremsstrahlung. The result (for Cu, but virtually *material independent*) is that the ablation depth is approximately equal to $40(I\tau^{1.5}/\lambda)^{1/2}$ nm, where λ is the wavelength (in centimeters). The plasma temperature is approximately equal to $3(I\lambda\sqrt{\tau})^{1/2}$ eV, a number that is useful for calculating X-ray emission (for photolithography). The directed velocity of neutral atoms is $0.6(I\lambda\sqrt{\tau})^{1/4}\,\text{cm}/\mu\text{s}$; however, ions are ejected at a $\geqslant 3$-times-higher velocity due to plasma voltages. In summary, one now has an extension of earlier results *down* into the $\geqslant 1$ GW/cm^2 range, below which plasma ablation converts into (*material-independent*) thermal or photochemical vaporization (see Phipps and Dreyfus, 1992).

Basic Relationships. Surface absorber ablation theory (Phipps et al., 1988) is developed from the work of Kidder (1968, 1971) and others (e.g., Basov et al., 1968; Krokhin, 1971; Caruso et al., 1966; Nemchinov, 1967), which formed the foundation of our understanding of laser-fusion hydrodynamics.

The principal assumptions used in the surface-absorber theory are as follows:

- One-dimensional flow
- Inverse bremsstrahlung heating mechanism
- All incident light employed to support the ablation flow
- Mach-1 flow (Chapman–Jouguet condition, $M = 1$)
- Ideal gas ($\gamma = 5/3$)
- Macroscopic charge neutrality ($n_e = Zn_i$)
- Self-regulating plasma opacity, giving unity optical thickness $S = 1$ at the laser wavelength, after a brief transition time τ_1

The assumption that inverse bremsstrahlung is the dominant plasma heating mechanism implies irradiance I is below the level (0.1–1 PW/cm^2, or 10^3–10^4 PW/m^2) required for dominance by anomalous (i.e., noncollisional) absorption processes (see Hughes, 1979).

The following three equations describe the physical problem:

$$S = \alpha c_s \tau \tag{59}$$

$$I = [M(M^2 + 3)/2]\rho_a c_s^3 \tag{60}$$

and

$$\alpha = \frac{CZ^3(Z+1)^{3/2}\lambda^2}{A^{7/2}}\frac{\rho_a^2}{c_s^3} \tag{61}$$

Equation (61) reexpresses the inverse bremsstrahlung absorption formula (57) in terms of the hydrodynamic variables ρ_a and c_s by employing the additional expressions:

$$\rho_a = (Am_p/Z)n_e \tag{62}$$

and

$$c_s = \left[\frac{\gamma(Z+1)kT_e}{Am_p}\right]^{1/2} \tag{63}$$

In Eq. (60), I is in physical rather than practical units, ρ_a is the ablation plasma mass density, and constant C has units $\text{L}^6\cdot\text{M}^{-2}\cdot\text{T}^{-3}$, with numerical value 1.136×10^{37} (cgs) or 1.136×10^{43} (SI).

When Eqs. (59)–(61) are solved, there results a fully transient theory in which the ablation pressure varies slowly with time during the evolution of the laser pulse, according to

$$\begin{aligned} p_a &= p_0, \qquad \tau < \tau_1 \\ p_a &= (\tau_1/\tau)^{1/8} p_0, \qquad \tau \geqslant \tau_1 \end{aligned} \tag{64}$$

where

$$p_0 = \frac{(1+\gamma M^2)}{\gamma} \frac{[(Am_p/Z)^{1/3} n_{ec}] I^{2/3}}{[M(M^2+3)/2]^{2/3}} \tag{65}$$

is the maximum ablation pressure that results from achievement of the critical density for $\tau < \tau_1$ early in the pulse, during the ablation.

The time τ_1 is given by

$$\tau_1 = \frac{I^{2/3} A^{7/2}}{2^{2/3} C Z^3 (Z+1)^{3/2} \lambda^2 \rho_a^{8/3}} \tag{66}$$

For convenience, we reexpress the transition time τ_1 using practical units for I:

$$\tau_1 = C_1 \frac{I^{2/3} A^{5/6} \lambda^{10/3}}{Z^{1/3} (Z+1)^{3/2}} \tag{67}$$

where the constant $C_1 = 1.05 \times 10^{-4}$ (cgs) or 1.05 (SI).

Two different sets of predictions for ablation variables (e.g., pressure, temperature, velocity, and mass ablation rate) result depending on whether $\tau \gtrless \tau_1$. The time τ_1 is so short compared to laser pulses normally used in LIMA work (e.g., pulse durations greater than 1 ps for KrF lasers, or 100 ps for Nd lasers) that the added complication of carrying along both sets of predictions for $\tau \gtrless \tau_1$ in the present work is not justified. We will just carry the relationships for $\tau \geqslant \tau_1$, keeping in mind that $\tau < \tau_1$ governs the field of laser fusion [for both sets of relationships, see Table II of Phipps et al. (1988)].

These results may be used to predict many of the interesting ablation parameters with good accuracy over a broad range of laser wavelengths (0.25–10 μm), pulse durations (up to 1 ms), and irradiances. Employing the conditions $S = 1$, $M = 1$, etc. listed at the beginning of this subsection gives the following set of relationships, the basis of our work in this chapter:

pessure $$p_a = 5.83 \frac{\Psi^{9/16}}{A^{1/8}} \frac{I^{3/4}}{(\lambda\sqrt{\tau})^{1/4}} \quad \text{dyn/cm}^2 \tag{68}$$

(with SI variables, the correct coefficient to obtain Pa is 1.84×10^{-4});

temperature $$T_e = 2.98 \times 10^4 \frac{A^{1/8} Z^{3/4}}{(Z+1)^{5/8}} (I\lambda\sqrt{\tau})^{1/2} \quad \text{K} \tag{69}$$

(with SI variables, the correct coefficient is 2.98×10^3);

density $$n_e = 3.59 \times 10^{11} \frac{A^{5/16}}{Z^{1/8}(Z+1)^{9/16}} \frac{I^{1/4}}{(\lambda\sqrt{\tau})^{3/4}} \quad \text{cm}^{-3} \tag{70}$$

(with SI variables, the correct coefficient to obtain m^{-3} is 1.135×10^{15});

ablation rate $$\dot{m} = 2.66 \frac{\Psi^{9/8} I^{1/2}}{A^{1/4} \lambda^{1/2} \tau^{1/4}} \quad \mu\text{g}\cdot\text{cm}^{-2}\cdot\text{s}^{-1} \tag{71}$$

(with SI variables, the correct coefficient to obtain $\mu\text{g}\cdot\text{m}^{-2}\cdot\text{s}^{-1}$ is 26.6); and

velocity $$c_s = 1.37 \times 10^6 \frac{A^{1/8}}{\Psi^{9/16}} (I\lambda\sqrt{\tau})^{1/4} \quad \text{cm/s} \tag{72}$$

(with SI variables, the correct coefficient to obtain m/s is 4.33×10^7). The ablation pressure p_a, electron temperature T_e, and sound speed c_s are evaluated in the Region I absorption zone, where laser light is converted into plasma pressure.

The parameter

$$\Psi = \frac{A}{2[Z^2(Z+1)]^{1/3}} \tag{73}$$

is a function of A and Z, and its magnitude is often ≈ 1. Among these quantities, the impulse coupling coefficient,

$$C_m = \int_{-\infty}^{\infty} d\tau p_a(\tau)/\Phi$$

is predicted to within a factor of 1.5 for a broad range of experimental data above plasma threshold in vacuum.

Data for $\dot{m}$ are predicted quite well in the high irradiance limit, but ablation depth $x_v = \dot{m}\tau/\rho$ is not predicted so well, especially at low intensities, as we discussed in developing conditions II and IV, because the heated surface

continues to emit material after the laser pulse has ceased (see Kelly and Rothenberg, 1985). Many laser pulses (e.g., CO_2) have a long, low-irradiance tail, which extends the vaporization time and complicates modeling. With a correction due to charge acceleration, ion velocities seem to be well predicted (see Phipps, 1989; also Section 4A.3, below).

Heat Conduction and Reradiation. In the high-irradiance regime, heat is mainly transported to the target via plasma blackbody radiation. Depending on density, temperature, and laser irradiance, bremsstrahlung and/or electron thermal conduction may also be important or even dominant. Because "high irradiance" in the context of laser ablation is still well below the values where nonclassical transport applies [approximately, $I \geqslant 100\,\mathrm{TW/cm^2}$ (or $10^{18}\,\mathrm{W/m^2}$) on target (see Pearlman and Anthes, 1975)], we consider only classical transport here. At irradiance levels appropriate for laser fusion, a "flux limitation" adjustment must be applied to the classical heat conduction formula (see, e.g., Max et al., 1980). We now derive typical magnitudes for heat transport variables in order to assess their importance in typical situations.

Electron Thermal Conduction. Heat transfer by thermal conduction in a plasma is mainly due to electrons because of their small mass and high velocity, and is given by

$$\mathbf{Q} = -K\nabla T \tag{74}$$

The classical electron thermal conductivity is given by (see Manheimer and Colombant, 1982; Spitzer, 1967):

$$K = K_0 T_e^{5/2} \tag{75}$$

watts per unit length, where (in cgs)

$$K_0 = 1.95 \times 10^{-11}\delta_t/Z\ln\Lambda \qquad \text{watts!} \tag{76}$$

or (SI)

$$K_0 = 1.95 \times 10^{-9}\delta_t/Z\ln\Lambda.$$

In Eq. (76), δ_t is a tabulated function of charge state Z that varies from 0.23 to 0.79 as Z varies from 1 to 16 (Spitzer, 1967), and $\ln\Lambda$ is the Coulomb logarithm defined in Eqs. (31) and (56). The heat flux transferred over a dimension equal to the laser focal spot radius is about (Phipps et al., 1988)

$$Q = 1.78 \times 10^4\, A^{7/16} f(Z)(I\lambda\sqrt{\tau})^{7/4}/d_s \qquad \mathrm{W/cm^2} \tag{77}$$

For SI units yielding $\mathrm{W/m^2}$, the correct coefficient in Eq. (77) is 563. The function

$$f(Z) = \delta_t Z^{13/8}/(Z+1)^{35/16} \tag{78}$$

is nearly a constant, varying from 0.05 to 0.18 as Z varies from 1 to 16, and returning to a value of 0.07 when $Z = 100$. Taking $I = 1\,\mathrm{GW/cm^2}$ ($10\,\mathrm{TW/m^2}$) and $I\lambda\sqrt{\tau} = 5\,\mathrm{W\cdot s^{1/2}\cdot cm^{-1}}$ ($500\,\mathrm{W\cdot s^{1/2}\cdot m^{-1}}$) for typical laser ionization microprobe conditions, $A = 12$ (carbon), $f(Z) = 0.1$, and $d_s = 2\,\mu\mathrm{m}$, the heat flux Q due to electron thermal conduction will be on the order of $0.44\,\mathrm{GW/cm^2}$ ($4.4\,\mathrm{TW/m^2}$). It is readily appreciated that the size of this flux approaches that of the absorbed laser flux.

Blackbody Irradiance. For an optically thick plasma (that is, one which is dense enough to be opaque to its own radiation), the emitted flux will be

$$\mathbf{Q} = \sigma\varepsilon T^4 \tag{79}$$

where ε is the emissivity. In the case of a perfect blackbody at 7 eV ($T = 11{,}605\,\mathrm{K/eV}$), $Q = 0.25\,\mathrm{GW/cm^2}$ ($2.5\,\mathrm{TW/m^2}$). This situation will occur, for example, in the high-pressure region very near the target surface. It is seen that the magnitude of this flux also approaches that of the absorbed laser flux, so that radiation and thermal conduction can both be important means of conducting heat to the target in high-irradiance LIMA work.

Bremsstrahlung Irradiance. For wavelengths or densities for which the plasma is *not* optically thick, classical bremsstrahlung emission describes the plasma's self-irradiance, rather than the blackbody formula. Appropriately, this is characterized by a volumetric rather than a surface source density (Allen, 1973):

$$i_B = \left(\frac{64\pi}{3}\right)\left(\frac{\pi}{6}\right)^{1/2}\left(\frac{e^6Z^2}{hc^3m_e}\right)\left(\frac{kT_e}{m_e}\right)^{1/2} n_e n_i \qquad \mathrm{erg\cdot cm^{-3}\cdot s^{-1}} \tag{80}$$

or

$$i_B = 1.425 \times 10^{-34} Z(T_e^{1/2}) n_e^2 \qquad \mathrm{W/cm^3} \tag{81}$$

The coefficient in Eq. (81) should be 1.425×10^{-40} for SI parameters, to yield $\mathrm{W/m^3}$. For a 7 eV plasma with electron density $n_e = 10^{20}\,\mathrm{cm^{-3}}$ ($10^{26}\,\mathrm{m^{-3}}$), $i_B = 0.4\,\mathrm{GW/cm^3}$ ($0.4\,\mathrm{PW/m^3}$). To compare these results, we note that the chief blackbody self-emission color per unit frequency interval for this plasma [see Eq. (18)] is at 63 nm wavelength, that Eq. (57) gives $1/\alpha = 8\,\mathrm{nm}$ absorp-

tion length for this color, and that $Q/i_B \approx 6$ nm. The difference between these values is a proper integration over the bremsstrahlung spectrum. Further, it is important to realize that LTE may not always apply well enough to establish the concept of T_e. Bremsstrahlung is the dominant type of plasma self-emission in Region III (see Figure 4A.1), yet it is small in comparison with the laser irradiance.

Adiabatic Expansion Theory: Thickness and Dimensionality of the Absorption Zone. The theory that led to Eqs. (68)–(72) is derived for one-dimensional expansions. However, it is intuitively clear that LIMA work sometimes involves two-dimensional expansions because of the small laser spot diameters used in this work. As mentioned previously, the phenomena concerning *laser coupling* to the target are considered to be correctly treated by one-dimensional theory when the standoff distance, x_I, of the absorption layer from the target is small compared to the laser spot diameter d_s on the target.

In the rare case when this is not so, the dimensionality corrections involved (Mora, 1982; Phipps et al., 1988) are very small, being proportional to $(x_I/d_s)^{1/9}$, and would amount to reduction of the pressure predicted by the one-dimensional laser coupling theory by at most a factor of 2 even in the extreme case $x_I/d_s = 300$.

In order to determine the standoff distance x_I, we follow the analysis of Manheimer and Colombant (1982), taking the distance between the absorption layer and the target surface x_I to be the thermal gradient scale length in Region I over which thermal convection and thermal conduction are balanced.

$$\tfrac{5}{2}\rho v C T = -K\frac{dT}{dx} \tag{82}$$

Since [see Eq. (75)] $K = K_0 T^{5/2}$, and using $v = c_s = \sqrt{(\gamma kT/Am_p)}$, we can integrate the resulting equation to find

$$x_I = 0.032\frac{K_0(A^{1/2})}{k^{3/2}[(\gamma/m_p)^{1/2}]}\frac{T^2}{n} \tag{83}$$

or, with $\ln\Lambda = 7$,

$$x_I = 5.5 \times 10^5[\delta_t(A^{1/2})/Z]T^2/n_e \quad \text{cm}$$

or (SI) (84)

$$x_I = 5.5 \times 10^9[\delta_t(A^{1/2})/Z]T^2/n_e \quad \text{m}$$

Note that Eqs. (84) have the form $x \propto T^2/n$, which is characteristic of a coulombic mean free path. Now, it only remains to substitute Eqs. (69) and (70) for T and n into Eq. (84) to obtain (in cgs).

$$x_I = 1365\left[\frac{\delta_t A^{7/16}Z^{5/8}}{(Z+1)^{11/16}}\right](I^{3/4}\lambda^{7/4}\tau^{7/8}) \quad \text{cm}$$

or (SI) (85)

$$x_I = 43\left[\frac{\delta_t A^{7/16}Z^{5/8}}{(Z+1)^{11/16}}\right](I^{3/4}\lambda^{7/4}\tau^{7/8}) \quad \text{m}$$

By taking the function $g(z) = \delta_t Z^{1/4}/(Z+1)^{7/8} = 0.13$ [it varies only slightly from 0.12 to 0.13 as Z varies from 1 to 16 (see Spitzer, 1967)] and substituting Eq. (72) for c_s, the time for collapse of the absorption zone pressure after the laser pulse, $t_I = x_I/c_s$, stated in Eq. (13), results.

It is clear that the dimensionality that applies to laser coupling in Region I can be assessed from the ratio x_I/d_s, which should be $\ll 1$ for a one-dimensional expansion. That this is normally the case can be seen by substitution of typical irradiation parameters. For example, substitution of $\lambda = 248$ nm, $I = 10\,\text{GW/cm}^2$, $\tau = 10$ ns, $A = 30$, and $Z = 1$ gives $x_I = 200$ nm, much smaller than laser spots.

Adiabatic Expansion Theory. At some distance $x = x_T$, plume expansion eventually makes a transition to multidimensional flow, even when laser coupling can be described as one-dimensional. In order to better understand the plasma plume expansion, we will ignore heat input and reradiation outside the absorption zone in Region I, and consider the predictions of adiabatic expansion theory. In such an expansion, the volume available to a fixed total number of particles expanding from the original perimeter at the flow-transition distance x_I depends only on the flow dimensionality a:

$$1 < a < 3 \tag{86}$$

Then the density

$$n(x)/n(x_I) = (x/x_T)^{-a} \tag{87}$$

We showed in the discussion surrounding Eq. (3) that theory predicts $a = 20/9 = 2.22$ whereas experiment shows $a \approx 2.5$. For an ideal gas, $\gamma = 5/3$, so

$$(p/p_T) = (n/n_T)^{\gamma} = (x/x_T)^{-5a/3} \tag{88}$$

whence

$$T(x)/T(x_T) = (n/n_T)^{2/3} = (x/x_T)^{-2a/3} \tag{89}$$

Since $\alpha \propto n^2/T^{3/2}$,

$$(\alpha/\alpha_T) = (x/x_T)^{-a} \tag{90}$$

Integrating along the laser beam path from infinity (where $x = \infty$ and $I = I_\infty$) to position x then gives

$$\frac{I(x)}{I_\infty} = \exp\left\{-\left[\frac{\alpha_T x_T}{(a-1)}\right]\left(\frac{x_T}{x}\right)^{[a-1]}\right\} \tag{91}$$

a function that has a scale thickness

$$x_{\text{abs}} = \left[\frac{\alpha_T}{a-1}\right]^{1/(a-1)} x_T^{a(a-1)} \tag{92}$$

If we take $x_T = (1/\alpha_T)$,

$$x_{\text{abs}} = \left(\frac{1}{a-1}\right)^{1/(a-1)} \frac{1}{\alpha_T} \tag{93}$$

Choosing $a = 2.5$ for the dimensionality of the flow in Regions II–IV to agree with experiment, we find $x_{\text{abs}} = 0.77\,(1/\alpha_T)$, where α_T is the inverse bremsstrahlung absorption coefficient for the laser wavelength in Region I. This was stated earlier without proof.

Shock Heating and Other Redistribution Processes. When picosecond duration or shorter pulses are used, one may ask whether the surface-absorber ablation theory we have presented applies or not. One notices, for example, that mass ablation rates are not predicted well. Several effects that have not been considered in deriving the basic theory may come into play to extend the heated region and dissipate incident heat flux. These include:

- Thermal conduction
- UV and X-ray heating of the target
- Hot-electron heating with front velocity, v_{hot}
- Shock heating

Of these, the last is the most important. Thermal conduction can develop a high velocity for picosecond pulses, but not high enough to penetrate a significant amount of material. X-ray heating can be shown to be less significant than shocks, and the hot-electron source term is weak until irradiance reaches the laser fusion regime [10 TW/cm^2 (100 PW/m^2) or so, outside the range of interest for most laser ablation work.

Shocks are important energy sinks for short pulses even at modest laser fluence levels. For such short pulses, the acoustic intensity will be $I_a = p^2\tau/\rho$, and mechanical coupling efficiency I_a/I can be quite good. We assume the sound wave is launched into the target material with intensity I_a and an attenuation coefficient α_a, propagating a distance $c_s\tau$ during the laser pulse. The fraction of the acoustic intensity that goes into solid material heating is given by

$$Q_s/I_a = c_s\tau\alpha_a \tag{94}$$

where

$$\alpha_a \equiv 1/(c_s\tau_{\text{B}}) \tag{95}$$

so that

$$Q_s/I_a = (\tau/\tau_{\text{B}}) \tag{96}$$

We have used the symbol τ_{B} for the acoustic relaxation time of the medium at the acoustic frequency $\omega_a = 2\pi/\tau$ induced by the laser pulse, because it can be found in the literature of stimulated Brillouin scattering (SBS) (see e.g., Heiman et al., 1978). The relaxation time

$$\tau_{\text{B}} = (2\pi/\eta)(c/\omega_a)^m \tag{97}$$

is a function of the material viscosity η and the acoustic frequency ω_a, which we take as determined by the laser pulse width that launches the shock, $\omega_a = 2\pi/\tau$. The coefficient m also varies with frequency:

$$m = 2/[1 + (\omega_a\tau_0)^2] \tag{98}$$

Based on the results of Heiman et al. (1978), we estimate that, for glasses as an example, where $\tau_0 \approx 50$ ps, $m \to 0$ at $\tau \approx 5$ ps, and that $\tau_{\text{Bmin}} \approx 50$ ps. Values for other materials will vary. Thus, a condition for inapplicability of our analysis is:

$$\tau \ll \tau_{\text{B}} \tag{99}$$

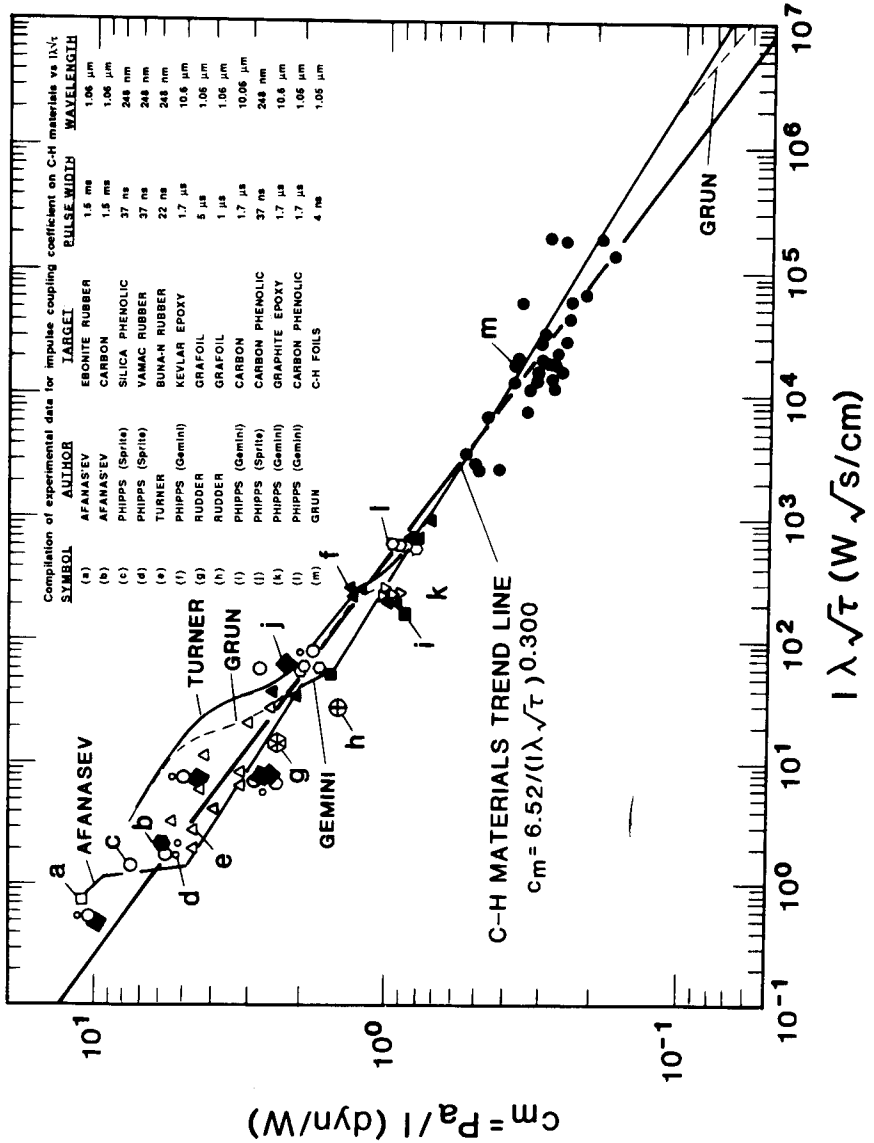

in the target material. The second condition, which must occur simultaneously to invalidate the analysis, is that the thickness $c_{\text{solid}}\tau$ be significant compared to the ablation depth during the pulse, $x_v = \dot{m}\tau/\rho$. They may be stated as

$$\dot{m} \ll \rho c_{\text{solid}} \tag{100}$$

For many solids, $\rho c_{\text{solid}} \approx 10^6\,\text{g}\cdot\text{cm}^{-2}\cdot\text{s}^{-1}$ ($10^7\,\text{kg}\cdot\text{m}^{-2}\cdot\text{s}^{-1}$). Since we nearly always deal with ablation rates that are smaller than this value, condition (99) is the limiting criterion. The foregoing can then be summarized as saying that we do not expect our theory to model picosecond and shorter pulses.

4A.2. EXPERIMENTAL RESULTS FOR HIGH IRRADIANCE

Figure 4A.5, reproduced from Phipps et al. (1988), shows how well the theory predicts vacuum surface impulse at high irradiance. Laser wavelengths represented in the figure are 10.6, 3, and 1.06 μm and 248 nm. Also represented are pulse lengths from 500 ps to 1.5 ms, and irradiances from 3.5 MW/cm^2 to 30 TW/cm^2. The data shown describe interaction with nonmetallic materials, but data from metals are fit equally well. The steps in the data fit show how changes in ionization state Z affect Ψ and thus C_m, which occur as laser irradiance increases. We can estimate the charge state Z with sufficient accuracy for calculating Ψ from, e.g., Eq. (23), if it is not otherwise known.

Note that we have plotted the impulse data vs. the scaling parameter $I\lambda\sqrt{\tau}$. This particular choice of parameter is suggested by Eq. (68) and the instantaneous relationship $C_m = p_a/I$.

4A.2.1. Mass Loss Rate

Figure 4A.6 shows the excellent agreement of the high-irradiance theory with measurements of $\dot{m}$ from the work of several authors (Yamanaka et al., 1986; Shirsat, et al., 1989; Gupta and Kumbhare, 1984). In the figure, the data of Yamanaka et al. are taken as the norm. Normalization adjustments are on the order of 30%.

The *lowest* irradiance represented on the graph is 1×10^{11} W/cm^2 in the data of Gupta and Kumbhare, and the highest 4×10^{14} W/cm^2 in the data

Figure 4A.5. Graph illustrating good agreement between an extensive compilation of experimental data for high-irradiance vacuum impulse coupling coefficient on C—H type materials vs. the parameter $I\lambda\sqrt{\tau}$. All Phipps, Rudder, and Turner references may be found in Phipps et al. (1988). Other references are Afanas'ev et al. (1969) and Grun et al. (1983).

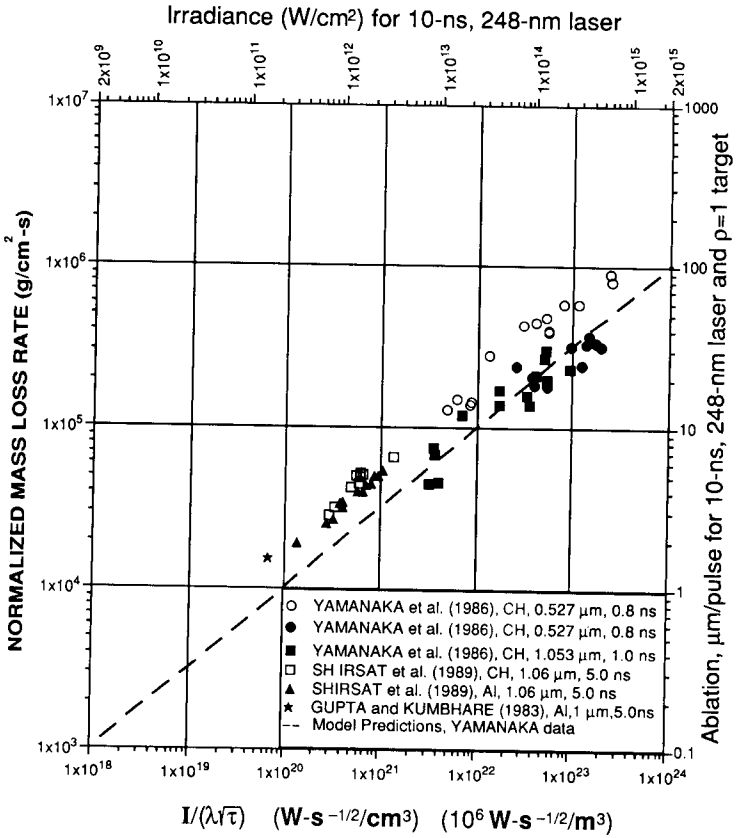

Figure 4A.6. Compilation of mass loss rate for high irradiance, compared to the Eq. (71) prediction. Mass loss is adjusted slightly to compensate for differences in atomic mass A and ion charge number Z, e.g., $C_{\text{Yamanaka}} = \Psi^{9/8}/A^{1/4} = 0.384$; see Eq. (71). Other data are adjusted for different conditions of atomic mass A and charge state Z by multiplying published $\dot{m}$ by $C_{\text{Yamanaka}}/C_{\text{data}}$ in order to make a comparison of data from widely different experimental conditions possible.

of Yamanaka et al. Note that we have plotted the mass loss data vs. the scaling parameter $I/(\lambda\sqrt{\tau})$, as suggested by Eq. (71).

4A.2.2. Ablation Depth

Our success in modeling $\dot{m}$ at high irradiance gives us confidence that we might also be able to approximately model high-irradiance measurements

of ablation depth:

$$x_v = \int_{-\infty}^{\infty} \frac{dt}{\rho} \dot{m} \approx \dot{m}\tau/\rho \qquad \text{cm} \tag{101}$$

Here, because $\dot{m}\tau \propto (I\tau^{3/2}/\lambda)^{1/2}$ [see Eq. (71)], the suggested plotting variable is $I\tau^{3/2}/\lambda$. Of course, exact modeling requires careful numerical calculations specific to each circumstance (see, e.g., Balazs et al., 1991).

We exclude data that do not at least approximately satisfy each of the conditions I–IV. The most frequent reason for excluding data from Figures

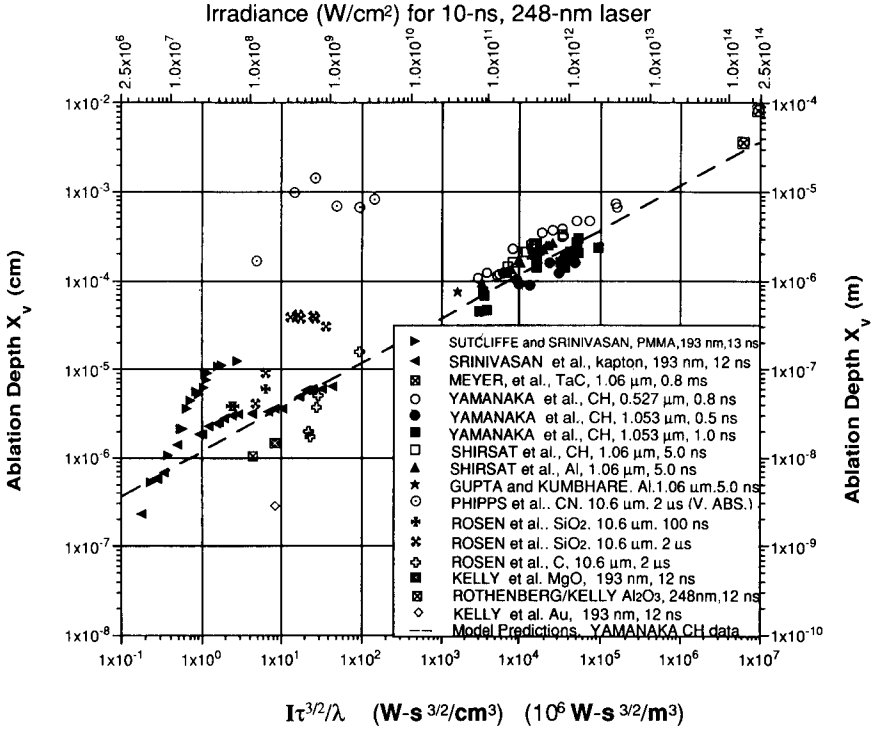

Figure 4A.7. Compilation of ablation depth data for high irradiance, compared to the Eq. (101) prediction. Ablation depth is adjusted slightly to compensate for differences in atomic mass A and ion charge number Z. The normalization is made to the conditions of Yamanaka as a standard by multiplying the published value of x_v by the factor $C2_{\text{Yamanaka}}/C2_{\text{data}}$, where $C2 = C/\rho$, ρ being the target solid mass density. One volume absorber data set is included for comparison, that of Phipps et al. (1990) [symbol ⊙], and one surface absorber set taken in air, that of Srinivasan et al. (1986a). Other data are the same as in Figure 4A.6, except for the addition of Rosen et al. (1988), Rothenberg and Kelly (1984), and Kelly et al. (1985).

4A.6 or 4A.7 was that the data were taken at insufficient irradiance to guarantee plasma dominance of the interaction (condition III) (e.g., Chuang et al., 1988). The next most frequent reasons were that the data were taken in air (condition I) or that the target was a volume absorber rather than a surface absorber (condition II).

Figure 4A.7 shows the results of this effort. In addition to the $\dot{m}$ data references given previously and the exceptional data discussed below, data are taken from Meyer et al. (1973), Kelly et al. (1985), and Rothenberg and Kelly (1984), for a total of 16 data sets. In cases where at least one point (typically the highest intensity point) of a data set crosses over into the parameter space that satisfies all the conditions, we have plotted the entire set.

The data of Meyer et al. (1973) [symbol ⊠] that we used shown in Figure 4A.7 were taken in vacuum, but no difference was seen when background pressure was as high as 0.2 torr (27 Pa) of O_2 or H_2. Meyer and coworkers' 25 ns carbon data were also modeled well, but they were not plotted in the figure because the additional points could not be seen in the data cluster at midrange of $I\tau^{3/2}/\lambda$.

We have also included three examples in Figure 4A.7 that violate one of our conditions strongly. The first, a volume-absorber data set [symbols ⊙] (see Phipps et al., 1990; Rosen et al., 1988) that violates condition II, shows the extent of ablation enhancement that is possible at low irradiance near plasma threshold in volume absorbers. These data represent the largest ablation depth per joule yet reported at any laser wavelength, as well as the largest momentum coupling coefficient C_m in a homogeneous target material.

The second, which is the polyimide set at the very short 193 nm wavelength, from Srinivasan et al. (1986b) [symbol ◀], gives excellent agreement with the model and is included to make the following point. While an air environment changes the interaction physics so much that the analysis in this chapter should be irrelevant—and, indeed, some impulse measurements in air show strong disagreement with measurements in vacuum—at irradiance above plasma threshold, but low enough to avoid forming laser-supported detonation waves (LSD waves) in the atmosphere above the target, very strong absorbers like kapton at 193 nm (surface absorbers) still seem to give the right answer. The LSD wave threshold at 1 bar for 10.6 μm lasers on aluminum is just under 1 GW/cm^2 (Beverley and Walters, 1976). The spectrophotometric absorption depth $1/\alpha$ for kapton at the 193 nm UV wavelength and standard temperature and pressure (STP) is 230 Å (Sutcliffe and Srinivasan, 1986).

The third set (from Sutcliffe and Srinivasan, 1986) [symbol ▶] is identical to the first, except that the target material is PMMA. This data set also violates our plasma ignition limit by about a factor of 10 at its lowest irradiance level. However, at irradiances where the data can be compared, it is interesting to note how small the region of volumetric absorption need

be to change the character of the ablation toward "volume" from "surface." The 193 nm absorption depth $1/\alpha$ is about 100 times larger with PMMA as compared to kapton—but still only 2.2 μm. However, the resulting ablation depth for the same irradiance is noticeably larger with PMMA than with kapton.

At high irradiance, *all* absorbers in vacuum coalesce to the behavior predicted by the dashed line in Figure 4A.7. As was explained in Section 4A.1.3, under the high temperature and pressure associated with high irradiance, the relatively long spectrophotometric absorption depths characteristic of volume absorbers shrink to resemble metallic absorption depths.

A lot of the scatter in Figure 4A.7 at low irradiance could well be due to modeling uncertainty: it is difficult to guess the values of $\langle A \rangle$ and $\langle Z \rangle$ that are required to apply the theory, and they are not given.

In summary, Figure 4A.7 shows it is possible to model x_v for surface absorbers over a 7 orders of magnitude range in the parameter $I\tau^{3/2}/\lambda$, including about a factor of 50 in laser wavelength, and at least 6 orders of magnitude in pulse duration from nanosecond to millisecond duration pulses, using a simple scaling formula. The analysis predicts ablation depth within a factor of 2 when $I\tau^{3/2}/\lambda > 50\ \mathrm{W \cdot s^{3/2} \cdot cm^{-3}}$ (500 $\mathrm{kW \cdot s^{3/2} \cdot m^{-3}}$), corresponding to irradiances above about 1 GW/cm^2 for 12 ns KrF lasers. This explains the choice of irradiance in the heading of Section 4A.1. For lower irradiance, the prediction becomes progressively poorer, as plasma physics no longer dominates surface chemistry. The x_v modeling may apply in air in some cases.

4A.3. ION ACCELERATION IN THE LOW-DENSITY PLUME

4A.3.1 Experiments

This section concerns what happens in Region IV of Figure 4A.1. Figure 4A.8, based on the ion velocity measurements of von Gutfeld and Dreyfus (1989), Eidmann et al. (1984), Gregg and Thomas (1966a,b), and Dreyfus (1991), demonstrates that there is good agreement with the velocity trend predicted by the model, but it is consistently found that a multiplier amounting to about $\sqrt{10}$ must be used to shift the prediction upward and match the measurements. The falloff at $I\lambda\sqrt{\tau} \approx 1$ is forseeable, as the area of validity for the present theory has been violated, e.g., power density is too low for inverse bremsstrahlung to be the major energy input (≤ 1 GW/cm^2).

It is concluded that, over a wide range of high-irradiance values in vacuum, something accelerates the ions, increasing their energy by a factor of 10 between the time of their creation in the ablation layer and their detection

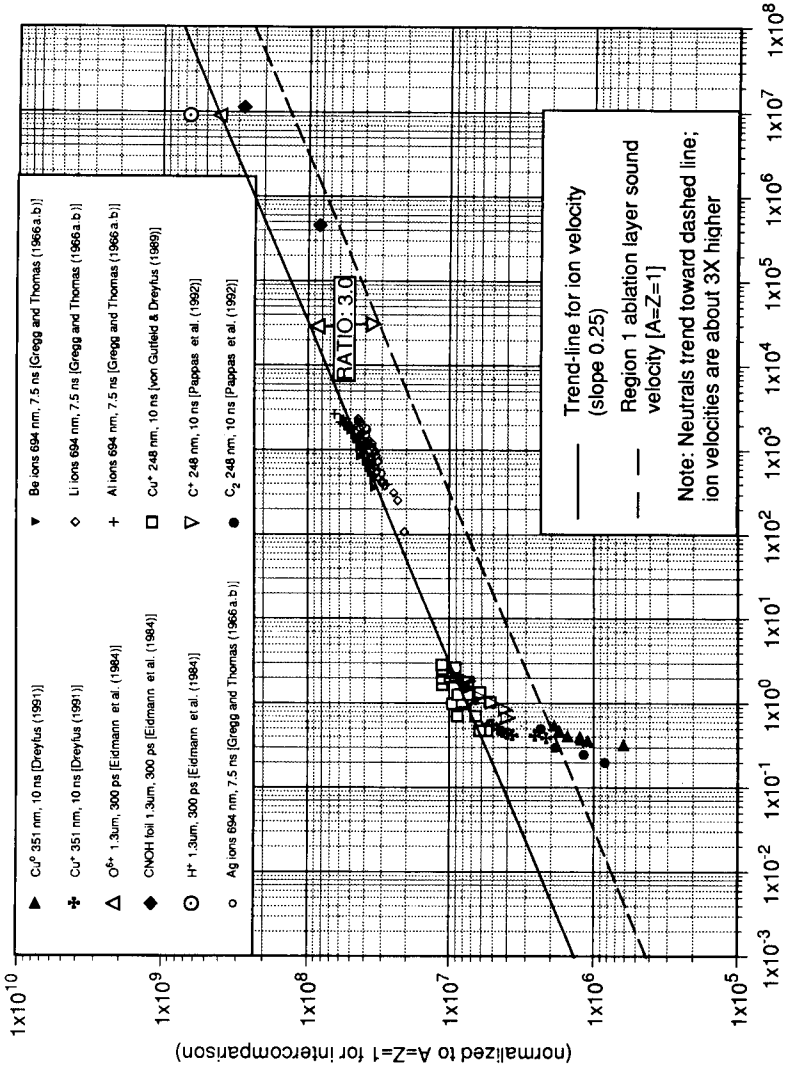

Figure 4A.8. Compilation of ion velocities in the high-irradiance regime, illustrating the point that velocity predicted by Eq. (72) for Region I seems to be consistently augmented by a multiplicative factor on the order of $\sqrt{10}$ in the plasma plume.

in the plasma plume. The loss of this acceleration at the lower boundary of the high-irradiance region is clearly seen in the Dreyfus (1991) copper ion data.

We note that the velocity of some neutral species falls on the same (accelerated) trend line as the ions [e.g., CN from polyimide at 248 nm wavelength (see Srinivasan and Dreyfus, 1985)]. This result suggests that these species gain energy, presumably due to photochemical ablation rather than a thermal one. We have plotted the CN data to illustrate this point, even though the species are not ions and are below the high-irradiance boundary.

If one appeals only to expansion work to find this energy, one finds from Kelly and Dreyfus (1988a) that the expected drift velocity u_K is close to the sound velocity that, from Eq. (5), is expected to show a $(x/x_T)^{-3/4}$ variation, i.e., a deceleration rather than an acceleration. Along with the approach of the experimental points to the theoretical prediction, note that only the neutral species approach the dashed line.

It is well known that very large ion-accelerating electric fields are created in high-irradiance laser–plasma interaction experiments. Langer et al. (1966) were possibly the first to notice suprathermal ion kinetic energy in vacuum laser irradiation experiments. They obtained C^{2+} ions with energies from 100 to 1000 eV from 10 GW/cm^2 laser irradiance (100 TW/m^2). They also recorded a threshold for formation of multiply charged C ions of 1.5 GW/cm^2 (15 TW/m^2). Multiply charged ions were always seen to have a narrower, higher energy spectrum. At 60 GW/cm^2 (0.6 PW/m^2), for example, C^{4+} ions with 1 keV energy were seen. The threshold for C^{4+} formation was 20 GW/cm^2. This corresponds to a *temperature* at their creation of only 64 eV (Allen, 1973).

Many other workers have also measured large laser-induced plasma voltages; e.g., Silfvast and Szeto (1977), Bergmann et al. (1980), and Cook and Dyer (1983) obtained 0.1–1 kV pulses from CO_2-laser-induced plasmas.

Bykovskii et al. (1972) observed typical Li^+ and D^+ ion drift-kinetic energies of 100 eV with 1 GW/cm^2 (10 TW/m^2) irradiation of LiD targets in vacuum. At 10 GW/cm^2 (100 TW/m^2), they saw Li^{2+} ions for the first time with a characteristic energy of 270 eV, whereas the Li^+ and D^+ ions showed a double-peaked distribution at about 120 and 300 eV, respectively, with tails extending up to 700 eV. With heavier ZrH targets at the same irradiance, Zr^{5+} ions were created with typical energy 2.5 keV, and the Zr^+ spectrum was essentially flat, rising slightly between 100 eV and 2.5 keV. Bykovskii et al. (1972) characterized these energy spectra as being much higher than thermal energy (about 15 eV for the LiD experiment). They explained these results by appealing to an accelerating field arising from hot electrons leaving the plasma. Their data is reproduced in Figure 4A.9.

David and Weichel (1969) noticed that $T_e \approx 10\, T_{plasma}$, in experiments with 1 GW/cm^2 irradiance on carbon.

Bykovskii et al. (1971) earlier observed clear evidence for separate

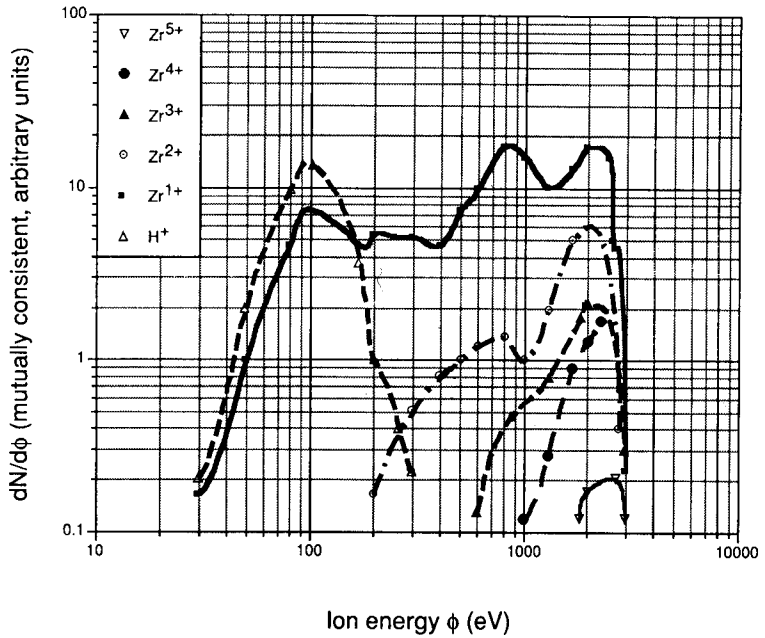

Figure 4A.9. Reproduction of Figure 3 of Bykovskii et al. (1972) showing the ion energy spectrum obtained in 1 μm wavelength laser ablation of zirconium hydride at 10 GW/cm^2 irradiance (100 TW/m^2). Where one would expect a temperature of about 15 eV for these irradiation parameters, very substantial suprathermal behavior is observed (used by permission).

"thermal" ($\approx$ 10 eV) and "accelerated" ($\approx$ 100 eV) time-of-flight (TOF) ion peaks at $I = 8$ GW/cm^2 (80 TW/cm^2) irradiance ($\lambda = 1.06\,\mu$m; $\tau = 15$ ns) with aluminium targets. The hot peak tended to be multiply charged ions. With 10 TW/cm^2 irradiance, these workers created 35 keV Co^{25+} ions. In their experiments, the threshold for this acceleration is clearly an irradiance of $I_{\text{thresh}} = 500$ MW/cm^2 (5 TW/m^2). Bykovskii et al. (1972) estimate that the fraction represented by the accelerated ions n_{i*} is

$$f_i = n_{i*}/n_i \approx D_e/d_s \tag{102}$$

This ratio is about 10^{-5} in the laser absorption zone, for KrF lasers and 100 μm diameter spots. Bykovskii et al. (1969) observed certain random anisotropies in the angular distribution of the ejected ions.

Inoue et al. (1970) were perhaps the first to observe beamlike behavior in the accelerated ions, in experiments producing 70 eV C^{2+} ions from poly(ethylene) with a ruby laser ($\lambda = 694.3$ nm) and irradiance around 2 TW/cm^2.

Bykovskii et al. (1971) also saw beamlike behavior, with ions ejected progressively closer to the target normal at $I > I_{\text{thresh}}$ in laser–target interactions. The measurements of Gupta et al. (1986) add further support to the picture of acceleration and ion beam narrowing. At 268 nm irradiances of 0.5–10 TW/cm^2, fast and slow aluminum ion peaks were clearly seen. Flux measurements showed the slow peak to be nearly isotropic, whereas the fast peak ions were clearly confined to a narrow cone around the target-normal.

Workers in laser fusion—where irradiance levels exceed 10 TW/cm^2 (100 PW/m^2)—are accustomed to seeing a ratio $f_T = T_*/T \approx 8$–20 (Haines 1979), with a population of "hot electrons" at least as large as

$$f_e = \frac{n_{e*}}{n_e} = \frac{(e\phi/kT_e)^{1/2}\exp(-e\phi/kT_e)}{\pi^{1/2}}\left(1 + \frac{1}{2e\phi/kT_e}\right) \tag{103}$$

In Eq. (103), $e\phi/kT_e$ is the ratio of the charge separation potential to the thermal energy in consistent units; Eq. (103) is derived by integrating a single Maxwellian energy distribution from $e\phi/kT_e$ to ∞ (Pearlman and Dahlbacka, 1977). At irradiance levels we often utilize in LIMA work, Eq. (103) provides a broadly applicable estimate of the hot fraction.

The work of Akhsakhalyan et al. (1982), one of the few instances in which the energy distribution was measured with irradiance as low as 1 GW/cm^2 at $\lambda = 1\,\mu$m, clearly shows $f_T = T_*/T \approx 10$ with a total hot particle flux about 2×10^{-3} of the total particle flux.

4A.3.2. Theory and Modeling

The best general theoretical treatment is given by Hora's theory of so-called double layers (DLs) (see Hora et al., 1989; Eliezer and Hora, 1989). DLs become important in the corona or outer region of the laser–plasma system.

In LTE, one expects (as in our earlier discussion of Debye sheaths) these layers of positive and negative charges to generate a potential jump that is on the order of kT_e, depending on the magnitude of the density gradient scale length $L_n = n_e/\nabla n_e$.

At high irradiance, the electron velocity distribution that develops from laser–plasma heating is no longer described by LTE concepts. Instead of a single Maxwellian velocity distribution, one finds that separate "thermal" (cold) and "hot" components with temperatures T and T_*, respectively, can briefly coexist. The simultaneous existence of "hot" and "thermal" electrons in the corona region results in charge separation sufficient to strongly accelerate positive ions.

Physical mechanisms that can create this departure from LTE, causing the production of "hot" electrons and ions, include resonance absorption (Denisov, 1957), relativistic self-focusing, at very high irradiance (Hora, 1975),

and magnetic field effects; Afanas'ev and Kanavin (1983) predict generation of magnetic fields on the order of 10 kG (1 T) at 5 GW/cm^2 (50 TW/m^2) irradiance on a 100 μm diameter spot.

An idea of the predicted ratio of "hot" to "normal" particle number at laser fusion irradiance levels is obtained from the work of Forslund et al. (1977). Their theory is based partly on the theory of resonant absorption in laser fusion (beyond our scope here) and is partly empirically derived from two-dimensional relativistic particle simulations at five different wavelengths spanning the range from 0.7 to 3 μm. They found:

$$f_e = \frac{n_{e*}}{n_e} = 0.24\left[\left(\frac{I\lambda^2}{T}\right)^{1/2}\right] \tag{104}$$

For SI unit parameters, the coefficient is unchanged. If applied to the Akhsakhalyan et al. (1982) case, Eq. (103) would predict $f_e = n_{e*}/n \approx 8 \times 10^{-3}$, in rough agreement with what they observed.

However, the prediction of Forslund et al. for the temperature ratio $f_T = T_*/T$ is not correct for irradiance levels below about 100 TW/cm^2.

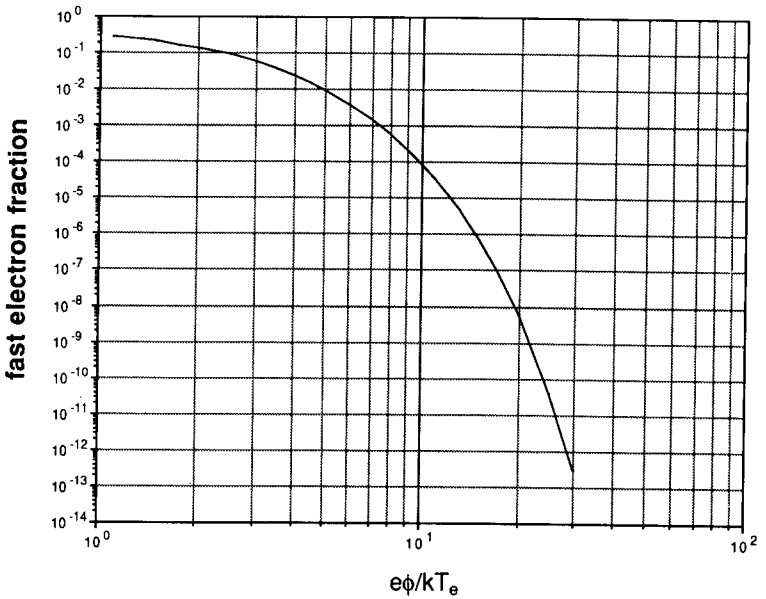

Figure 4A.10. A plot of the hot electron fraction given by Eq. (103) vs. the ratio $e\phi/kT_e$ defined in the text, for a Maxwellian velocity distribution of electrons in LTE.

Instead, one may use the theory of Eliezer and Hora (1989), which gives

$$(6f_T - f_T^2 - 1)^2 - 16f_T^2 \geq 0 \tag{105}$$

requiring that $f_T \geq 5 + \sqrt{24} = 9.9$.

The function f_e in Eq. (103) is plotted in Figure 4A.10. In the figure, we can see that a potential $e\phi/kT_e = 10$ times the thermal potential can be reached by $f_e = 10^{-4}$ of the total electron population of a single Maxwellian velocity distribution, about 20 times less than observed by Akhsakhalyan et al. (1982), reinforcing the idea that a complete non-LTE treatment would be better.

Afanas'ev et al. (1988) show that the electric field created should have a logarithmic dependence on D_e/d_s. Mulser (1971) proved that, while there is no question that plasma electric fields in high-irradiance experiments are capable of causing the ion acceleration that we see, the velocity *difference* between ions of different mass observed in TOF experiments *cannot* be explained by different forces acting on them in the accelerating field but must instead be due to irradiance inhomogeneities in the laser spot on target. Langer et al. (1966) showed that irradiance inhomogeneities could be deliberately manipulated via astigmatic focus to create anisotropic ion ejection patterns.

We now address acceleration in the experiment of von Gutfeld and Dreyfus (1989), as most relevant to problems that might arise in LIMA work. This problem has been previously addressed by Phipps (1989). We begin with the paper of Pearlman and Dahlbacka (1977), in which they reported observing laser-produced electric potentials on the order of 10 kV persisting for up to 200 times the laser pulse duration in a 50 ps laser–target irradiation experiment at $\lambda = 1.06$ μm wavelength. The development of a 30° fwhm ion beam with energy as large as 1 MeV was inferred from the data.

We believe that the physical mechanism for charge acceleration in the ablation experiment of von Gutfeld and Dreyfus (1989) is the same as in Pearlman and Dahlbacka's case. A suprathermal accelerating electric potential is set up between a separate "hot" component of the electron velocity distribution and the slower-moving ions, which are initially left behind—a topic that we introduced in our discussion of Region IV. The "hot" electron fraction escapes LTE simply by escaping the experiment before interactions with other particles have a chance to operate. The most energetic ions (of equal and opposite total charge) then accelerate up to the hot electrons, taking most of their energy as already described in Section 4A.1.2.

The experimental parameters of von Gutfeld and Dreyfus (see Table 4A.3) set this hot electron fraction at $f_e \approx 8 \times 10^{-4}$. If we insert this value into Eq. (102), we obtain a single Maxwellian acceleration factor $e\phi/kT_e = 9$ and

Table 4A.3. Self-Consistent Values for von Gutfeld and Dreyfus Experimental Parameters

Fluence Φ	$6\,\mathrm{J/cm^2}$
Material	Cu, $\rho = 8\,\mathrm{g/cm^3}$
Enthalpy	$H_v = 5300\,\mathrm{J/g}$
Emitted neutrals	$N_0 = 3.7 \times 10^{18}\,\mathrm{cm^{-2}}$
Escape fraction	$f_{esc} = 8 \times 10^{-4}$
Ionization fraction	$\eta = 1$
Target beam area	$\mathscr{A}_b = 0.02\,\mathrm{cm^2}$
Total emitted electrons	$N_e \mathscr{A}_b = 7.4 \times 10^{16}$
Escaping electrons	$f_{esc} N_e \mathscr{A}_b = 6 \times 10^{13}$
Ion divergence angle	$\phi_d = 40°$ fwhm
Ion burst duration	$\tau = 3\,\mu\mathrm{s}$
Escaping electron current	$\mathscr{J} = 3\,\mathrm{A}$
Ion potential	$e\phi = 38\,\mathrm{eV}$
Beam impedance	$Z = 160\,\Omega$ (ohms)
Probe distance	$x = 10\,\mathrm{cm}$
$n_i(x)$	$1 \times 10^{12}\,\mathrm{cm^{-3}}$
Velocity enhancement	$(e\phi/kT_e)^{1/2} = 3$
Temperature	$T_e = 4\,\mathrm{eV}$

note that $(e\phi/kT_e)^{1/2} \approx 3$ agrees with the ion velocity enhancement factor shown by the von Gutfeld and Dreyfus data (discussed in Section 4A.3.1). We also find that this value is consistent with the measurements of Bykovskii et al. (1972). We find that the von Gutfeld and Dreyfus irradiance, wavelength, and temperature values predict $f_e \approx 5 \times 10^{-4}$ via Eq. (103); Eq. (104) gives $e\phi/kT_e = 9.9$, also in excellent agreement with observation.

We can give a heuristic argument that allows prediction of the quantity $e\phi/kT_e$ from the particle mass ratio. First, we apply the constraint of current equality $[j_e = j_i]$, necessary for a steady potential, taking the energetic electron current to be limited by the ion thermal current:

$$n_{e^*} v_{e^*} = Z n_i v_i \tag{106}$$

Then, applying the twin conditions of LTE $[v_e = (m_i/m_e)^{1/2} v_i]$ and overall charge neutrality $[Zn_i = n_e]$ within the electron and ion thermal populations of Eq. (106) gives

$$(e\phi/kT_e)^{1/2} = (v_{e^*}/v_e = n_e/n_{e^*})\,[(m_e/m_i)^{1/2}] \tag{107}$$

or

$$f_e^2(e\phi/kT_e) = m_e/m_i \tag{108}$$

Now, applying (103), we find

$$\exp(e\phi/kT_e) = (m_i/\pi m_e)^{1/2}(e\phi/kT_e + \tfrac{1}{2}) \tag{109}$$

or

$$e\phi/kT_e = \tfrac{1}{2}\ln(m_i/\pi m_e) + \ln(e\phi/kT_e + \tfrac{1}{2}) \tag{110}$$

Because of the slow variation of the first logarithmic term, $e\phi/kT_e \approx 7$ within 15% for atoms ranging from copper to carbon. As an example, for a carbon plasma, Eq. (109) gives $e\phi/kT_e = 6.26$ and, for a copper plasma, $e\phi/kT_e = 7.32$. Therefore, the velocity ratio $(e\phi/kT_e)^{1/2} \approx 2.5$ over the same range of atoms.

These energetic electrons then attract and accelerate a cloud of ions from the thermal plasma. Given enough space, it is important to realize that these ultimately move at the same velocity as the electrons,

$$v_{e^*}|_{after} = v_{i^*} \tag{111}$$

slowing them down until the ions have effectively captured all the electrons' kinetic energy.

We further find that we can satisfy the requirements for energy conservation between the two energetic clouds,

$$m_e n_{e^*} v_{e^*}^2|_{before} = m_i n_{i^*} v_{i^*}^2|_{after} \tag{112}$$

in addition to Eqs. (106) and (108) as well as charge neutrality $[Zn_i = n_e]$, by requiring that

$$f_i = \frac{n_{i^*}}{n_i} = \left(\frac{Z}{e\phi/kT_e}\right) f_e \tag{113}$$

For copper ions, Eq. (113) gives $f_i = 1.5 \times 10^{-4}$ and $f_e = 1.1 \times 10^{-3}$, very close to observations and earlier estimates in this section.

The acceleration process further narrows the emitted ion beam—down to 20° fwhm in the von Gutfeld and Dreyfus experiment on copper targets, using KrF laser irradiation. At the same time, as the coulomb potential accelerates the ions, there exists a competing dilution process in which resonant charge exchange as well as classical ion–molecular collisions transfer the energy into the neutral cloud, i.e., there is a distinct energy gain by neutrals

as well. This is noted in Figure 4A.8 for the case of CN from polyimide (though this artifact may be explained instead by photochemical processes) and has been noted for Al from Al_2O_3 (Dreyfus et al., 1986c) and C_2 from PMMA (Srinivasan et al., 1986b). While these systems did not involve intense plasmas dissociating diatomics, there does exist a conflicting process in which plasma-induced dissociation eliminates many of the more energetic diatomics. The result of this selective dissociation is an apparent *slowing* (loss of kinetic energy) for the diatomics surviving (see Dreyfus et al., 1986c).

The foregoing considerations are capable of reproducing the key elements of the von Gutfeld and Dreyfus experiment. In Table 4A.3 we give the results of a self-consistent calculation that agrees with the reported aspects of that experiment (Phipps, 1989).

4A.4. MEASUREMENT TECHNIQUES IN THE LOW-DENSITY PLUME CREATED BY HIGH LASER IRRADIANCE

4A.4.1. Langmuir Probes

The Langmuir probe is one of the best known and—in general—best understood of plasma diagnostic techniques. Von Gutfeld and Dreyfus (1989) were among the first to apply this tool to the *quantitative* measurement of coronal plasma parameters in vacuum ablation experiments.

A Langmuir wire probe is deceptively simple, consisting of a dc-biased current probe inserted into the plasma [see Figure 4A.11 (from von Gutfeld and Dreyfus, 1989)]. It is a tool that is useful for exploring the instantaneous electron temperature and ion density in a thermal (Maxwellian, LTE) plasma. Ideally, the collected electron current I_e depends on the potential ϕ and the electron temperature according to (Chen, 1965)

$$I_e/I_0 = \exp(e\phi/kT_e) \tag{114}$$

when $\phi = (\phi_{probe} - \phi_{space})$ is positive so as to repel ions and collect electrons. Then, a plot of $\ln(I_e/I_0)$ vs. ϕ gives the electron temperature through the slope e/kT_e. The so-called space potential, ϕ_s, is the voltage assumed by the probe when it is allowed to float. In the work of von Gutfeld and Dreyfus, a value of $T_e \approx 2\,eV$ was determined at $x = 10\,cm$. Even though Eq. (69) predicts a value of 4 eV, ionization after the initial pulse and effects of the adiabatic expansion could easily have decreased T_e (T_e commonly falls to $\sim 1/3$ of the average ionization energy in a collisional plasma).

When the probe is biased negative, so as to collect ions, the ion density

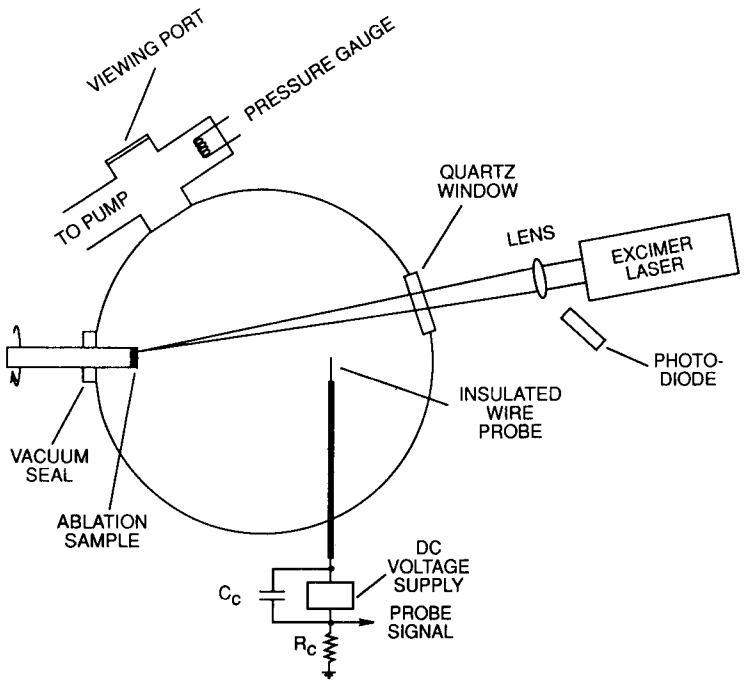

Figure 4A.11. Reproduction of Figure 1 of von Gutfeld and Dreyfus (1989) showing the arrangement for the Langmuir probe experiment (used by permission).

can be determined reliably from

$$n_i = \frac{1}{\mathscr{A}}\left\{\left[\frac{-4\pi m_i}{3_{e^3}}\frac{d(I_i^2)}{d\phi_p}\right]^{1/2}\right\} \quad cm^{-3} \tag{115}$$

where $\mathscr{A}$ is the probe area exposed to the plasma; I_i is the ion current; ϕ_p is the probe voltage; and m_i is the ion mass. Note that T_i is usually difficult to measure from the ion current characteristic, owing to the overlapping large electron currents at lower negative potentials.

TOF data are also available from the probe signals and offer valuable information about the nature and drift velocity of charged particles, ion charge states, etc.

Experimental Precautions:

Nondisturbance. In order not to disturb the thermal energy distributions being measured, care must be taken to limit the maximum instantaneous

electron or ion current withdrawn from the plasma, and not to cool the plasma by using an unduly large probe. These considerations lead to the use of a very-small-diameter wire for the probe, e.g., 75 μm in the work of von Gutfeld and Dreyfus. The electron current limitation can be observed experimentally when the apparent slope obtained from Eq. (114) starts to change with the current.

Probe Heating. One has to be careful not to draw such a large ion current as to cause thermionic emission from the probe. This regime is commonly only a problem for dc plasmas, but not for the few microseconds of a laser-generated plasma.

Sheath Thickness. It is important to calculate the thickness of the plasma sheath that forms around the probe: the collecting area $\mathscr{A}$ in Eq. (115) is the sheath area, which is greater than the geometric area of the probe by an amount that depends on plasma density and temperature. This correction acts to reduce the apparent ion density.

Termination Impedance. The Langmuir probe is a very delicate charge collection device with a small capacitance, so that a too-large termination resistor (used to convert current into voltage at the oscilloscope) will cause the probe voltage to vary during the measurement, generating faulty data. A simple Ohm's law calculation avoids this problem.

Negative Ion Species. Unfortunately, not all ions are positive. In ablation plasma measurements, TOF will usually allow discrimination between the negative ions and the electrons. It is important to locate the probe far enough from the ablation surface to take advantage of this discrimination capability.

4A.4.2. Time of Flight

Probably the earliest instances of kinetic energy measurements of laser-produced ions is the work of Linlor (1963) and that of Gregg and Thomas (1966a,b) with a 7.5 ns ruby laser (694.3 nm). In the latter work, irradiances from about 5 GW/cm^2 to 0.4 TW/cm^2 (50 TW/m^2–4 PW/m^2) were incident on a 220 μm diameter illumination spot, producing ion velocities from 7×10^6 to 3×10^7 cm/s (70–300 km/s) and ion kinetic energy as large as 2 keV. Materials investigated were Li, LiH, Be, C, Al, S, Zn, and Ag. These data are reproduced, in part, in Figure 4A.8. It was found that ion velocity varied with irradiance according to

$$v_i \propto I^b \tag{116}$$

where the coefficient $0.19 \leqslant b \leqslant 0.43$, the smallest value applying to Ag, and

the largest to Al. We note that Eq. (70) predicts $b = 0.250$, in the middle of this range. In this experiment, no reflecting potentials were used.

One of the most important features about the expected signal in TOF experiments is the result of Kelly and Dreyfus (1988a,b). Since

$$n_i \propto 1/t \tag{117}$$

where

$$v_i = x/t \tag{118}$$

and

$$|dv_i| = x\,dt/t^2 \tag{119}$$

then, for a density-sensitive detection system such as LIF, one obtains a counterintuitive result that the detected signal will be proportional to v^4:

$$\begin{aligned} ds \propto n_i v_i f_i(v)\,dv &\propto (x^2/t^4)\exp\{-[mx^2/(2kT_i t^2)]\}\,dt \\ &= (v^4/x^2)\exp(-mv_i^2/2kT_i)\,dt \end{aligned} \tag{120}$$

For a flux-sensitive detector, the response even has a v^5 dependence.

In the high-intensity regime, sophisticated TOF experiments have augmented simple TOF with a retarding potential electrostatic filter, pulsed deflection voltage, and extraction field (Vertes et al., 1988).

4A.4.3. Laser-Induced Fluorescence

Laser-induced fluorescence (LIF) is also an extremely useful diagnostic for laser ablation plasmas and is the only way to get certain kinds of information. In the pioneering work of Dreyfus et al. (1986a), this technique made it possible to detect and measure the energy distributions of the species AlO, C_2, and CN during KrF irradiation of aluminum oxide and polyimide (kapton).

The technique has also been used to advantage in measuring velocity distributions and relative populations of excited-state and fine-structure levels of atoms sputtered from surface samples (Zare, 1984).

Table 4A.4 shows examples of laser wavelengths that have been used to detect particular species by selectively inducing fluorescence. Observables with this technique include drift velocity (kinetic energy), rotational temperature, and vibrational temperature. As an example of the latter work, Dreyfus et al. (1986b) were able to use LIF to determine both the rotational and vibrational energies of AlO diatomics, as well as the translational kinetic energy of AlO and Al.

Table 4A.4. Laser-Induced Fluorescence (LIF) at High Irradiance: Species and Wavelengths

Species	Pump Wavelength (nm)	Detection Wavelength (nm)	Reference
CN	385–388.3 (dye)	422	Dreyfus et al (1986a)
C	230.1–230.2	230	Dreyfus et al. (1987)
C_2	230 (doubled dye)	230	Dreyfus et al. (1986c)
C_2	248 (KrF)	470	Walkup et al. (1985)
C_3	230	230	Dreyfus et al. (1987)
Al	248	396.2	Rothenberg and Kelly (1984)
AlO	447–450	—	Dreyfus et al (1986)

Koppman et al. (1986) used the LIF technique to assess the velocity, energy, and density of Li and Al ions created by ruby laser irradiation of an Li/Al sandwich at 1.5 GW/cm^2 irradiance. The purpose of the experiment was to create short ion beam bursts for injection into magnetic fusion plasma machines.

4A.4.4. Other Ion Diagnostics

Emission spectroscopy (Venugoplan, 1971), resonance ionization (Bonnie et al., 1987), and laser beam deflection by optical inhomogeneities (Chen and Yeung, 1988; Dreyfus et al., 1986b) have been used in ion source plasma diagnostics. Vertes et al. (1990) has given an excellent review of the subject of measuring and modeling plasma processes in ion sources.

PPTD. Dreyfus et al. (1987) developed the pulsed photothermal deformation (PPTD) technique for measuring energy deposited in surfaces by focused laser light. This technique, which utilizes the thermal deformation of the irradiated surface as a diagnostic, should be as useful for ablation work in vacuum as it was for their work in air. PPTD is extremely sensitive, with a noise level corresponding to 20 nJ absorbed.

"Laser Microprobe" Spacial Mapper. As regards this instrument, see Huie and Yeung (1985), Steenhoek and Yeung (1981), and Yappert et al. (1987). Spacially and temporally resolved maps of ablated atom concentrations over the target surface were obtained by interrogating the laser-generated plume with a second laser beam of appropriate wavelength chosen for selective absorption by the ablated species and recording the transmitted beam on a vidicon. Time gating at 50 μs intervals was provided by a Bragg cell. For

maximum tunability to match different species, the interrogating laser was an argon-ion-laser-pumped pulsed dye laser.

Thomson Parabola. The so-called Thomson parabola instrument (Olsen et al., 1973) seems not to have been used yet in laser ablation experiments, although it has been extremely useful in inertial confinement fusion. In this instrument, parallel electric and magnetic fields oriented perpendicular to the ion velocity give combined deflections that, combined with TOF information, are able to uniquely define the charged particles charge, mass, and energy without changing the particle energy. The device gets its name from the fact that the electrostatic deflection $x_e \propto Z/(Av_i^2)$, while the magnetic deflection $x_m \propto Z/(Av_i)$, so that each charged particle traces out a distinct parabola moving toward the origin as time evolves on the instrument screen,

$$x_e/x_m^2 = A/Z \tag{121}$$

with only mass-to-charge ratio A/Z determining the shape of the parabola.

Faraday Cage. As a closing note, we mention the very interesting and novel ion diagnostics work of Siekhaus et al. (1986). They used a Faraday cage (with very small openings for the laser beam) surrounding the ablation experiment to measure the total electron charge emitted during 1.06 and 0.35 μm vacuum irradiation of insulator and semiconductor surfaces at pulse widths from 1 to 40 ns. Irradiance ranged from about 15 MW/cm^2 up to 15 GW/cm^2—at the upper end of their data, definitely within the high-irradiance regime. The sample was held by a grounded metal holder inside a collector can, surrounded by an outer shield can. Both of the latter cans were maintained at a common variable bias potential in the range $\pm$ 300 V. Materials studied were CdTe, ZnS, NaCl, SiO_2, CeF_3, W, and GeO_2. In the 1 ns work at the Nd:YAG third harmonic on ZnS and SiO_2, the total charge measured at 10 J/cm^2 fluence was about 1 μC, or 6.2×10^{12} electrons . We see that this figure is about 10^{-4} of $N_e \mathscr{A}_b$, which we calculated in Table 4A.3. Siekhaus et al. found the emitted charge increased strongly with laser target fluence Φ. They found

$$Q/Q_0 = (\Phi/\Phi_0)^m \tag{122}$$

with $m = 9$ for SiO_2, suggesting that the factor-of-3 more irradiance would have achieved the emission we calculate for the von Gutfeld and Dreyfus experiments on copper at $\Phi = 6$ J/cm^2. Unfortunately, Siekhaus and colleagues did no measurements on metals at high irradiance. Space charge limitation may also have affected their results.

4A.5. SUMMARY AND CONCLUSIONS

Laser ablation and plasma formation are discussed in the high-irradiance regime, as it applies to LIMA work. Four regions of the laser–target interaction are visualized to occur as one moves away from the target, mainly distinguished by progressively longer collision times.

Four conditions were listed and explained, all of which must be satisfied for the high-irradiance analysis to apply. These included irradiance above the plasma formation threshold, a vacuum environment, surface absorption, and sufficiently small targets. The concept of local thermodynamic equilibrium (LTE) was discussed as it applies to the physics of pulsed laser–plasma interaction.

A straightforward analysis based on plasma physics was shown to give the expected mass ablation rate and total ablation depth. We reviewed experimental data on ablation rate, ablation depth, and ion velocity from a wide range of lasers and target materials and found that the analysis presented in this chapter provided a very convenient way of organizing such data.

We further found that vacuum laser ablation rate and ablation depth for many materials that are surface absorbers could be predicted quite well over a very broad range of laser parameters.

In addition, we found that many ion experiments could be predicted quantitatively if the velocity given by LTE plasma physics theory were enhanced by a constant factor $\sqrt{g} \approx \sqrt{10}$, derived from measurements of ion flux at a distance from the target in one instance.

Finally, we reviewed a number of measurement techniques for the low-density plasma plume created in a laser ablation experiment, including PPTD, Langmuir probes, Faraday cages, laser microprobes, TOF, and laser-induced fluorescence (LIF), and summarized results obtained with them.

ACKNOWLEDGMENTS

The authors gratefully acknowledge very helpful discussions with Prof. E. Matthias of the Free University, Berlin, and the travel support of NATO Research Grant SA.5-2-05(CRG.880020)1133/90/AHJ-514.

REFERENCES

Afanas'ev, Yu. V., and Kanavin, A. P. (1983). *Kvantovaya Elektron.* (*Moscow*) **11**, 423–426; *Sov. J. Quantum Electron.* (*Engl. Transl.*) **14**, 292–294 (1984).

Afanas'ev, Yu. V., Basov, N. G., Krokhin, O. N., Morachevskii, N. V., and Sklizkov, G. V. (1969). *Zh. Tekh. Fiz.* **39**, 894–905; *Sov. Phys.—Tech. Phys.* (*Engl. Transl.*) **14**, 669–676 (1969).

Afanas'ev, Yu. V., But, S. M., and Kanavin, A. P. (1988). *Kvantovaya Elektron.* (*Moscow*) **15**, 744–746; *Sov. J. Quantum Electron.* (*Engl. Trans.*) **18**, 474–475 (1988).

Akhsakhalyan, A. D., Bityurin, Yu. A., Gaponov, S. V., Gudkov, A. A., and Luchin, V. I. (1982). *Zh. Tekh. Fiz.* **52**, 1584–1589; *Sov. Phys.—Tech. Phys.* (*Engl. Transl.*) **27**, 969–973 (1982).

Allen, C. W. (1973). *Astrophysical Quantities*, 3rd ed., p. 33. Athlone Press, London.

Balazs, L., Gijbels, R., and Vertes, A. (1991). *Anal. Chem.* **63**, 314–320.

Basov, N. G., Gribkov, V. A., Krokhin, O. N., and Sklizkov, G. V., (1968). *Zh. Eksp. Teor. Fiz.* **54**, 1073–1080; *Sov. Phys.—JETP* (*Engl. Transl.*) **27**, 575–582.

Batanov, V. A., Bunkin, F. V., Prokhorov, A. M., and Fedorov, V. B. (1972). *Zh. Eksp. Teor. Fiz.* **63**, 586–608; *Sov. Phys.—JETP* (*Engl. Transl.*) **36**, 311–322 (1973).

Berchenko, E. A., Koshkin, A. V., Sobolev, A. P., and Fedyushin, B. T. (1981). *Kvantovaya Elektron.* (*Moscow*) **8**, 1582–1584; *Sov. J. Quantum Electron.* (*Engl. Trans.*) **11**, 953–955 (1981).

Bergmann, E. E., McLellan, E. J., and Webb, J. A. (1980). *Appl. Phys. Lett.* **37**, 18–19.

Beverley, R. E., III, and Walters, C. T. (1976). *J. Appl. Phys.* **47**, 3485–3495.

Bingham, R. A., and Salter, P. L. (1976a). *Int. J. Mass Spectrom. Ion Phys.* **21**, 133–140.

Bingham, R. A., and Salter, P. L. (1976b). *Anal. Chem.* **48**, 1735–1750.

Boland, B. C., Irons, F. E., and McWhirter, R. W. P. (1968). *J. Phys.* **B1**, 1180–1191.

Bonnie, J. H. M., Eenshuistra, P. J., and Hopman, H. J. (1987). *AIP Conf. Proc.* **158**, 133–142.

Book, D. L. (1989). In *AIP 50th Anniversary Physics Vade Mecum* (H. Anderson, ed.), p. 278. Am. Inst. Phys., New York.

Bykovskii, Yu. A., Dudoladov, A. G., Degtyarenko, N. N., Elesin, V. F., Kozyrev, Yu. P., and Nikolaev, I. N. (1969). *Zh. Eksp. Teor. Fiz.* **56**, 1819–1822; *Sov. Phys.—JETP* (*Engl. Transl.*) **29**, 977–978 (1969).

Bykovskii, Yu. A., Degtyarenko N. N., Elesin, V. F., Kozyrev, Yu. P., and Sil'nov, S. M. (1971). *Zh. Eksp. Teor. Fiz.* **60**, 1306–1319; *Sov. Phys.—JETP* (*Engl. Transl.*) **33**, 706–712.

Bykovskii, Yu. A., Vasil'ev, N. N., Degtyarenko, N. N., Elesin, V. F., Laptev, I. D., and Nevolin V. N. (1972). *Zh. Eksp. Teor. Fiz., Pis'ma. Red.* **15**, 308–311; *JETP Lett.* (*Engl. Transl.*) **15**, 217–220 (1972).

Carslaw, H. S., and Jaeger, J. C. (1959). *Conduction of Heat in Solids*, 2nd ed., p. 75. Oxford University Press (Clarendon), New York.

Caruso, A., Bertotti, B., and Giupponi, P. (1966). *Nuovo Cimento* **45**, 176–189.

Chen, F. F. (1965). In *Plasma Diagnostic Techniques* (R. H. Huddlestone and S. L. Leonard, eds.) Chapter 4, pp. 113–199. Academic Press, New York.

Chen, G., and Yeung, E. S. (1988). *Anal. Chem.* **60**, 864–868.

Chuang, T. J., Hiraoka, H., and Mödl, A. (1988). *Appl. Phys.* **A45**, 277–288.

Coles, J. N. (1976). *Surf. Sci.* **55**, 721–724.

Conzemius, R. J., and Capellen, J. M. (1980). *Int. J. Mass Spectrom. Ion Phys.* **34**, 197–271.

Cook, G., and Dyer, P. E. (1983). *J. Phys.* **D16**, 889–896.

David, C. D., and Weichel, H. (1969). *J. Appl. Phys.* **40**, 3764–3770.

Denisov, N. G. (1957). *Sov. Phys.—JETP (Engl. Transl.)* **4**, 544–550.

Dreyfus, R. W. (1991). *J. Appl. Phys.* **69**, 1721–1729.

Dreyfus, R. W., Kelly, R., and Walkup, R. E. (1986a). *Appl. Phys. Lett.* **49**, 1478–1480.

Dreyfus, R. W., Walkup, R. E., and Kelly, R. (1986b). *Radiat. Eff.* **99**, 199–211.

Dreyfus, R. W., Kelly, R., Walkup, R. E., and Srinivasan, R. (1986c). *Proc. Soc. Photo-opt. Instrum. Engi.* **710**, 46–54.

Dreyfus, R. W., McDonald, F. A., and von Gutfeld, R. J. (1987). *J. Vac. Sci. Technol.* **B5**, 1521–1527.

Duzy, C., Woodroffe, J. A., Hsia, J. C., and Ballantyne, A. (1980). *Appl. Phys. Lett.* **37**, 542–544.

Eidmann, K., Amiranoff, F., Fedosejevs, R., Maaswinkel, A. G. M., Petsch, R., Sigel, R., Spindler, G., Teng, Y., Tsakiris, G., and Witkowski, S. (1984). *Phys. Rev.* **A30**, 2568–2589.

Eliezer, S., and Hora, H. (1989). *Phys. Rep.* **172**, 339–458.

Eloy, J. F. (1974). *Bull. Inf. Sci. Tech., Commis. Energ. At. (Fr.)* **192**, 71–75.

Fabbro, R., Fournier, J., Ballard, P., Devaux, D., and Virmont, J. (1990). *J. Appl. Phys.* **68**, 775–784.

Figueira, J. F., Czuchlewski, S. J., Phipps, C. R., and Thomas, S. J. (1981). *Appl. Opt.* **20**, 838–841.

Forslund, D. W., Kindel, J. M., and Lee, K. (1977). *Phys. Rev. Lett.* **39**, 284–290.

Gaunt, J. A. (1930). *Proc. R. Soc. London* **A126**, 654–690.

Gill, D. H., and Dougal, A. A. (1965). *Phys. Rev. Lett.* **15**, 845–849.

Ginzburg, V. L. (1970). *The Propagation of Electromagnetic Waves in Plasmas*, 2nd ed., p. 36. Pergamon, New York.

Glickler, S. L., Shraiman, B. J., Woodroffe, J. A., and Smith, M. J. (1980). *Am. Inst. Aeronaut. Astronaut., 13th Fluid Plasma Dyn. Conf.*, Pap. 80–1320.

Golub', A. P., Nemchinov, I. V., Petrukhin, A. I., Pleshanov, Yu. E., and Rybakov, V. A. (1981). *Zh. Tekh. Fiz.* **51**, 316–323; *Sov. Phys.—Tech. Phys. (Engl. Transl.)* **26**, 191–196 (1981).

Gregg, D. W., and Thomas, S. J. (1966a). *J. Appl. Phys.* **37**, 2787–2789.

Gregg, D. W., and Thomas, S. J. (1966b). *J. Appl. Phys.* **37**, 4313–4316.

Grey Morgan, C. (1978). *Sci. Prog. (Oxford)* **65**, 31–50.

Grun, J., Obenschain, S. P., Ripin, B. H., Whitlock, R. R., McLean, E. A., Gardner, J., Herbst, M. J., and Stamper, J. A. (1983). *Phys. Fluids* **26**, 588–597.

Gupta, P. D., and Kumbhare, S. R. (1984). *J. Appl. Phys.* **55**, 120–124.

Gupta, P. D., Tsui, Y. Y., Popil, R., Fedosejevs, R., and Offenberger, A. A. (1986). *Phys. Rev.* **A33**, 3531–3534.

Haines, M. G. (1979). *Proc. Scott. Univ. Summer Sch. Phys.* **20**, 145–218.

Hauer, A. A., Forslund, D. W., McKinstrie, C. J., Wark, J. S., Hargis, P. J., Hamill, R. A., and Kindel, J. M. (1989). In *Laser Induced Plasmas and Applications* (L. J. Radziemski and D. A. Cremers, eds.), pp. 385–436. Dekker, New York.

Heiman, D., Hamilton, D. S., and Hellwarth, R. W. (1978). *Phys. Rev.* **B19**, 6583–6592.

Hora, H. (1975). *J. Opt. Soc. Am.* **65**, 882–890.

Hora, H., Min, G., Eliezer, S., Lalousis, P., Pease, R. S., and Szichman, H. (1989). *IEEE Trans. Plasma Sci.* **17**, 284–289.

Hughes, T. P. (1979). *Proc. Scott. Univ. Summer Sch. Phys.* **20**, 1–90.

Huie, C. W., and Yeung, E. S. (1985). *Spectrochim. Acta* **40B**, 1255–1258.

Inoue, N., Kawasumi, Y., and Miyamoto, K. (1970). *Plasma Phys.* **13**, 84–87.

Johann, J., Luk, T. S., Egger, H., and Rhodes, C. K. (1986). *Phys. Rev.* **A34**, 1084–1102.

Kelly, R., and Dreyfus, R. W. (1988a). *Nucl. Instrum. Methods* **B32**, 341–348.

Kelly, R., and Dreyfus, R. W. (1988b). *Surf. Sci.* **198**, 263–276.

Kelly, R., and Rothenberg, J. E. (1985). *Nucl. Instrum. Methods* **B7**, 755–763.

Kelly, R., Cuomo, J. J., Leary, P. A., Rothenberg, J. E., Braren, B. E., and Aliotta, C. F. (1985). *Nucl. Instrum. Methods* **B9**, 329–340.

Kidder, R. E. (1968). *Nucl. Fusion* **8**, 3–12.

Kidder, R. E. (1971). In *Proceedings of the International School of Physics, Course 48* (P. Caldirola and H. Knoepfel, eds.), pp. 306–352. Academic Press, New York.

Koppman, R., Refaei, S. M., and Pospieszczyk, A. (1986). *J. Vac. Sci. Technol.* **A4**, 79–85.

Kovalev, I. D., Maksimov, G. A., Suchkov, A. I., and Larin, N. V. (1978). *Int. J. Mass Spectrom. Ion Phys.* **27**, 101–137.

Krokhin, O. N. (1971). In *Proceedings of the International School of Physics, Course 48* (P. Caldirola and H. Knoepfel, eds.), pp. 278–305. Academic Press, New York.

Küper, S., and Stuke, M. (1989). *Appl. Phys. Lett.* **54**, 4–6.

Landau, L. D., and Lifschitz, E. M. (1958). *Statistical Physics*, p. 13. Pergamon, London.

Langer, P., Tonon, G., Floux, F., and Ducauze, A. (1966). *IEEE J. Quantum Electron.* **QE-2**, 499–506.

Linlor, W. I. (1963). *Appl. Phys. Lett.* **3**, 210–213.

Manheimer, W. M., and Colombant, D. G. (1982). *Phys. Fluids* **25**, 1644–1652.

Max, C. E., McKee, C. F., and Mead, W. C. (1980). *Phys. Rev. Lett.* **45**, 28–31.

Meyer, R. T., Lynch, A. W., and Freese, J. M. (1973). *J. Phys. Chem.* **77**, 1083–1092.

Montgomery, D. C., and Tidman, D. A. (1964). *Plasma Kinetic Theory*, pp. 33–37. McGraw-Hill, New York.

Mora, P. (1982). *Phys. Fluids* **25**, 1051–1056.

Mulser, P. (1971). *Plasma Phys.* **13**, 1007–1012.

Mulser, P., Sigel, R., and Witkowski, S. (1973). *Phys. Rep.* **6**, 187–239.

Nemchinov, I. V. (1967). *Prikl. Mat. Mekh.* **31**, 300–319; *J. Appl. Math. Mech.* (*Engl. Transl.*) **31**, 320–338 (1967).

Nogar, N. S. (1991). *Workshop Laser Albation Mech. Appl., Oak Ridge, Tennessee*, 1991. **389**, 3–11.

Olsen, N., Kuswa, G. W., and Jones, E. D. (1973). *J. Appl. Phys.* **44**, 2275–2283.

Otis, C. E., and Dreyfus, R. W. (1991). *Phys. Rev. Lett.* **67**, 2102–2105.

Pappas, D., Sanger, K., Cuomo, J., and Dreyfus, R. (1992). *J. Appl. Phys.* **72,** 3966–3970.

Pearlman, J. S., and Anthes, J. P. (1975). *Appl. Phys. Lett.* **27**, 581–585.

Pearlman, J. S., and Dahlbacka, G. H. (1977). *Appl. Phys. Lett.* **31**, 414–417.

Phipps, C. R. (1989). *Mechanical Effects Induced by Laser*, Gen. Lect. I, Euromech. 257 Conf. University of Aix-Marseille (unpublished).

Phipps, C. R., and Dreyfus, R. W. (1992). *Bull. Am. Phys. Soc.* [*2*] **37**, 83.

Phipps, C. R., Turner, T. P., Harrison, R. F., York, G. W., Osborne, W. Z., Anderson, G. K., Corlis, X. F., Haynes, L. C., Steele, H. S., and Spicochi, K. C. (1988). *J. Appl. Phys.* **64**, 1083–1096.

Phipps, C. R., Harrison, R. F., Shimada, T., York, G. W., Turner, T. P., Corlis, X. F., Steele, H. S., Haynes, L. C., and King, T. R. (1990). *Laser Part. Beams* **8**, 281–295.

Puell, H. (1970). *Z. Naturoforsch.* **25**, 1807–1815.

Raizer, Yu. P. (1977). *Laser-Induced Discharge Phenomena*, p. 9. Consultants Bureau, New York.

Ramendik, G. I., Manzon, B. M., and Tyurin, D. A. (1987). *Talanta* **34**, 61–67.

Rose, D. J., and Clark, M. (1961). *Plasmas and Controlled Fusion*, p. 67. Wiley, New York.

Rosen, D. J., Mitteldorf, J., Kothandaraman, G., Pirri, A. N., and Pugh, E. R. (1982a). *J. Appl. Phys.* **53**, 3190–3200.

Rosen, D. J., Hastings, D. E., and Weyl, G. M. (1982b). *J. Appl. Phys.* **53**, 5882–5890.

Rosen, D. J., Rollins, C. R., and Chen, J. (1988). Report SR-334. "Issues in Laser Propulsion." Physical Science, Inc., Andover, Mass. (unpublished).

Rothenberg, J. E., and Kelly, R. (1984). *Nucl. Instrum. Methods* **229**(B1), 291–300.

Shirsat, T. S., Parab, H. D., and Pant, H. C. (1989). *Laser Part. Beams* **7**, 795–805.

Siekhaus, W. J., Kinney, J. H., Milam, D., and Chase, L. L. (1986). *Appl. Phys.* **A39**, 163–166.

Silfvast, W. T., and Szeto, L. H. (1977). *Appl. Phys. Lett.* **31**, 726–728.

Smith, W. L. (1978). *Opt. Eng.* **17**, 489–503.

Spitzer, L. (1967). *Physics of Fully ionized Gases*, 2nd ed., pp. 120–153. Wiley (Interscience), New York.

Spitzer, L., and Härm, R. (1953). *Phys. Rev.* **89**, 977–982.

Srinivasan, R., and Dreyfus, R. W. (1985). *Laser Spectrosc.* **7**, 396–400.

Srinivasan, R., Braren, B., and Dreyfus, R. W. (1986a). *J. Appl. Phys.* **61**, 372–376.

Srinivasan, R., Braren, B., Dreyfus, R. W., Hadel, L., and Seeger, D. E. (1986b). *J. Opt. Soc. Am.* **B7**, 785–791.

Srinivasan, R., Sutcliffe, E., and Braren, B. (1987). *Appl. Phys. Lett.* **51**, 1285–1287.

Steenhoek, L. E., and Yeung, E. S. (1981). *Anal. Chem.* **53**, 528–532.

Sutcliffe, E., and Srinivasan, R. (1986). *J. Appl. Phys.* **60**, 3315–3322.

Taylor, R. S., Singleton, D. L., and Paraskevopoulos, G. (1987). *Appl. Phys. Lett.* **50**, 1779–1781.

Ursu, I., Apostol, I., Barbulescu, D., Mihailescu, I. N., and Moldovan, M. (1981). *Opt. Commun.* **39**, 180–184.

Venugopalan, M., ed. (1971). *Reactions under Plasma Conditions*, Vol. 1, 367–542. Wiley, New York.

Vertes, A., and Juhasz, P. (1986). *Int. J. Mass Spectrom. Ion Process* **94**, 63–85.

Vertes, A., Juhasz, P., Jani, P., and Czitrovszky, A. (1988). *Int. J. Mass Spectrom. Ion Processes* **83**, 45–70.

Vertes, A., DeWolf, M., Juhasz, P., and Gijbels, R. (1989). *Anal. Chem.* **61**, 1029–1035.

Vertes, A., Gijbels, R., and Adams, F. (1990). *Mass Spectrom. Rev.* **9**, 71–113.

Viswanathan, R., and Hussla, I. (1986). *J. Opt. Soc. Am.* **B3**, 796–800.

von Gutfeld, R. J., and Dreyfus, R. J. (1989). *Appl. Phys. Lett.* **54**, 1212–1213.

Weyl, G. (1989). In *Laser Induced Plasmas and Applications* (L. J. Radziemski and D. A. Cremers, eds.), p. 25. Dekker, New York.

Yamanaka, C., Nakai, S., Yamanaka, T., Izawa, Y., Mima, K., Nishihara, K., Kato, Y., Mochizuki, T., Yamanaka, M., Nakatskuka, M., and Yabe, T. (1986). In *Laser Interaction and Related Phenomena* (H. Hora and G. Miley, eds.), pp. 395–419. Plenum, New York.

Yappert, M. C., Kimbrell, S. M., and Yeung, E. S. (1987). *Appl. Opt.* **26**, 3536–3541.

Zare, R. N. (1984). *Science* **226**, 298–303.